Genome Biology

METHODOLOGY

Open Access

scComm: a contrastive learning framework for deciphering cell–cell communications at single-cell resolution

Zijie Jin[1,2†], Zongli Tang[1,2†], Xinyi Li[1†], Kuangen Zhang[3], Zhengwei Xie[2,4*] and Ning Zhang[1,2,3,4*]

†Zijie Jin, Zongli Tang and Xinyi Li contributed equally to this work.

*Correspondence: xiezhengwei@hsc.pku.edu.cn; zhangning@bjmu.edu.cn

[1] Department of Immunology, School of Basic Medical Sciences, Health Science Center, Peking University, Beijing 100191, China
[2] Peking University International Cancer Institute, Health Science Center, Peking University, Beijing 100191, China
[3] Translational Cancer Research Center, Peking University First Hospital, Beijing 100034, China
[4] Yunnan Baiyao Group Co., Ltd., Kunming 650500, China

Abstract

Cell–cell communication regulates complex biological processes in multicellular systems. Existing scRNA-seq-based methods typically aggregate gene expression by clusters, overlooking within-cluster heterogeneity. We present scComm, a computational framework that infers cell–cell communications between individual cells using supervised contrastive learning. In simulations, scComm outperforms other methods and achieves up to 95% accuracy. Applied to colorectal cancer, it reveals cell–cell communications linked to PD-1 blockade response and tertiary lymphoid structures. In liver cancer, it identifies three novel tumor subtypes and angiogenesis-promoting neutrophil subtypes that have unique tumor microenvironments. scComm enables high-resolution cell–cell communication analysis, uncovering biological insights missed by existing approaches.

Keywords: Cell–cell communications, Single-cell resolution, Ligand-receptor pair selection, Supervised contrastive learning, Intratumoral heterogeneity, Tumor microenvironment

Background

Cell–cell communications (CCCs) regulate the dynamic coordination of biological processes in multicellular organisms between neighboring and distant cells [1–3]. Intercellular signaling involves the exchange of ligands, receptors, and downstream signaling molecules that allow cells to influence each other's behavior such as proliferation, differentiation, and migration. Characterizing these communication networks is crucial for understanding how cells cooperate to sustain normal tissue function and how their dysregulation leads to disease. The CCC events are primarily initiated through the binding of ligands released by sender cells to corresponding receptors on receiver cells, and can be inferred by analyzing the expression of genes encoding ligands and receptors [4]. Starting from 2015, several Ligand-Receptor (L-R) databases containing hundreds to

thousands L-R gene pairs have been built through literature curation and experimental validation [5–10].

Cell–cell communication inference methods generally follow one of two strategies: top-down or bottom-up. Top-down approaches first group cells into predefined clusters or cell types, then aggregate L-R expression within each group to infer communication between groups. In contrast, bottom-up approaches begin by inferring interactions between individual cells, and subsequently group cells based on the similarity of their communication profiles. While top-down methods, such as CellChat and CellPhoneDB [10–20], are computationally efficient, they ignore the cellular heterogeneity within clusters and often miss interactions involving rare or functionally distinct subpopulations. This limitation is particularly significant in tumor tissues, where malignant cells exhibit extremely high heterogeneity, making it challenging to classify them into definite functional subclusters and analyze CCC events related to tumor subclusters. Bottom-up methods can, in principle, capture this heterogeneity and reveal communication-defined cell communities that do not align with conventional cell type labels. However, current methods designed for inferring CCCs between individual cells generates an enormous volume of interaction information without filtering or statistical evaluation, making it difficult to distinguish biologically meaningful interactions from background noises. Without effective strategies to extract key CCC events, valuable biological insights may be overlooked. Thus, there is an urgent need for computational frameworks that can simultaneously evaluate CCCs without the constrain of prior clustering and identify the most informative interactions from the high-dimensional data. Another important challenge in CCC prediction lies in the variability of L-R databases. As highlighted by Dimitrov et al., CCC inference heavily depends on these prior-knowledge resources, yet existing databases differ substantially in their content [20]. Consequently, the choice of database can markedly influence the inferred interactions and their functional interpretation. Computational methods should be designed to ensure robustness against database selection.

To address these challenges, we introduce scComm, a bottom-up computational tool designed to infer CCCs at single-cell resolution. scComm applies a data-adaptive weighting and scoring module to assign weight to L-R pairs according to their importance and employs a supervised contrastive learning framework to detect significant CCC events. scComm demonstrates superior performances on the accuracy and sensitivity of CCC detection in both simulated datasets and eight real-world datasets. When applied to a colorectal cancer dataset, scComm reveals enhanced chemokine-mediated CCC activity associated with tertiary lymphoid structure formation, providing explanation for therapy responsiveness across three patient groups. This also demonstrates the capability of scComm in detecting cell-type level CCCs. Further, we apply scComm to a large liver cancer cohort collected by our lab and detect the novel neutrophil subtypes with distinct intercellular communication patterns that promote tumor angiogenesis, offering explanation for tumor progression and the poor prognosis. In addition, scComm identifies three novel tumor cell subtypes characterized by their interaction patterns and distinct tumor microenvironments, where the tumor subtype exhibiting low immune infiltration associates with higher malignancy. Notably, scComm quantifies the interaction scores

and describes the microenvironment for each single cell, providing as a CCC-based cell clustering tool in this study.

Results

Overview of the single-cell resolution CCC detection algorithm scComm

scComm takes a gene-by-cell expression matrix with annotated cell types from single cell RNA-seq data as input. It uses ligand-receptor (L-R) database as references to quantify the L-R pairs among single cells. The scComm workflow is organized into three modules (Fig. 1a). In the first module, we apply the data-adaptive strategy to assign weights to L-R pairs based on their likelihood determined by three factors: specificity, competitiveness, and activity. The specificity weight measures whether an L-R pair is enriched in particular cell groups using the term frequency-inverse document frequency (TF-IDF) method. The competitiveness weight assesses the binding potential of ligands and receptors. For instance, when multiple ligands target the same receptor, those with higher expression levels are more likely to engage in signaling. The activity weight measures the functional relevance of an L-R pair by analyzing the co-expression pattern of the receptor gene and associated transcription factors. A low activity weight suggests that the ligand and receptor genes are co-expressed by chance rather than participating in meaningful communication. This weighting process helps filter out L-R pairs with minimal impact on cell interactions and mitigates inconsistencies across different L-R databases. Notably, well-established L-R pairs, frequently observed in multiple databases, tend to have greater biological significance compared to rare or unvalidated pairs [20].

The second module calculates interaction scores for each cell pair across L-R pairs by multiplying the L-R pair's weight with the normalized geometric mean of the L-R gene expressions, based on the assumption that key L-R genes, often characterized by high expression levels, are more influential in intercellular communication, while those with lower expression may be less significant [21]. We adopt normalization to interaction scores to ensure that the relative expression levels of L-R pairs are accurately represented, mitigating the impact of extreme expression values. This module generates a comprehensive L-R pair-by-cell-by-cell interaction tensor with high dimensionality.

We apply a supervised contrastive learning framework for distinguishing significant CCC events from background noises (Fig. 1b, Methods). The goal of contrastive learning is to learn latent patterns among high-confidence CCC scores within the existing scoring framework. In the absence of ground truth for true CCC events, a data augmentation strategy is used to generate positive samples for contrastive learning, while cell label permutation is applied to construct negative samples. Feature embeddings of cell groups are obtained using a multilayer perceptron (MLP) encoder. The model is trained by minimizing the SupCon loss [22]. This contrastive learning framework enables the identification of significant CCC events at both the cell group and single-cell levels.

The final module outputting interaction data with three parts: 1) *cell–cell interaction score,* which is not symmetric, reflecting the directional feature of cell interactions, where the influence of cell A on cell B may differ from that of cell B on cell A. 2) *cell type/group aggregation,* which is an L-R pair-by-cell type/group interaction matrix. Each matrix entry represents the mean interaction score between cells belonging to

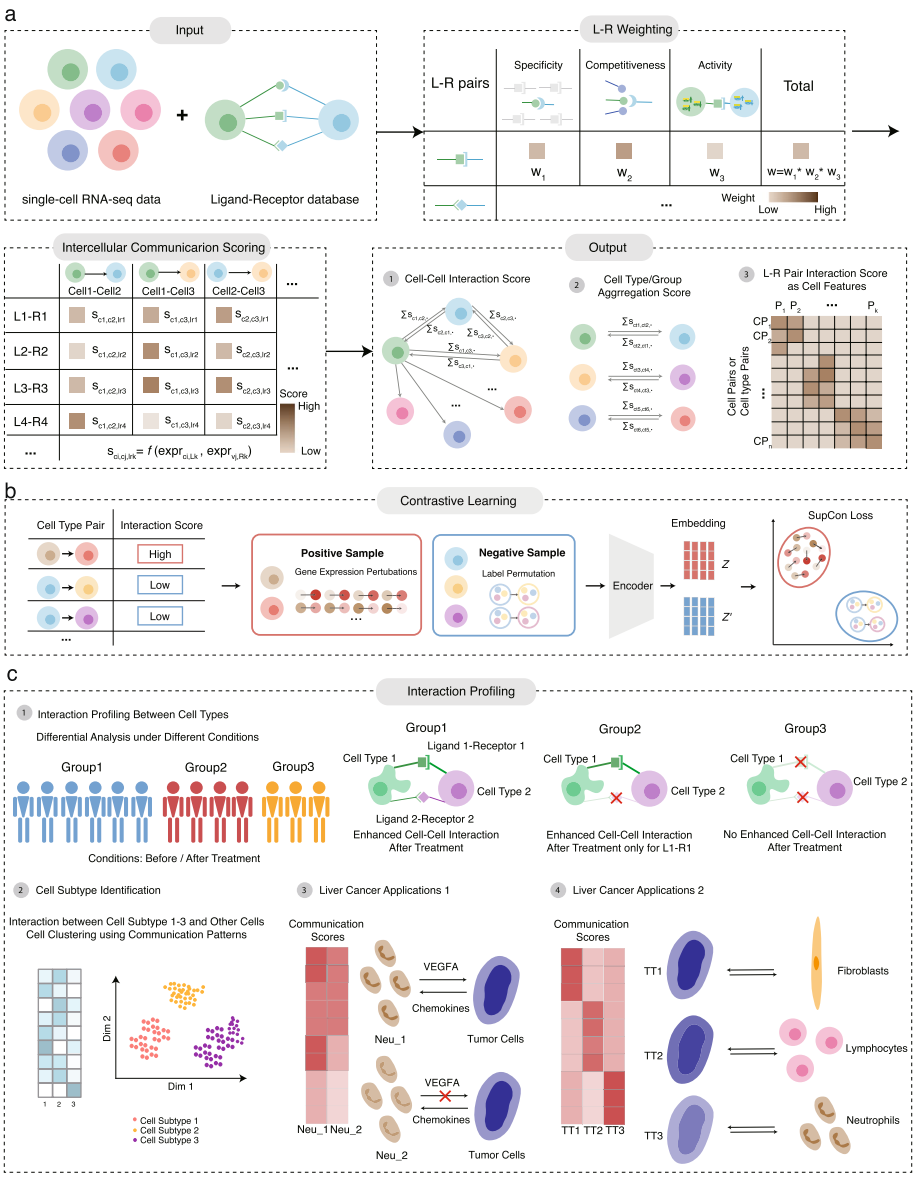

Fig. 1 scComm workflow. **a** The scComm pipeline integrates single-cell RNA gene expression data and a ligand-receptor (L-R) database to dynamically assign weights to each L-R pair according to their specificity, competitiveness, and downstream activity in this dataset. Cell–cell communication scores are calculated according to the gene expression and L-R pair weight. The resulting scoring matrix facilitates the assessment of aggregated interactions (1), aggregation to the cell type level or custom grouping (2), and inference of interaction patterns (3). **b** The supervised contrastive learning framework for identifying significant interacting cell pairs and/or cell type pairs. Cell type pairs having top 5% interacting score are regarded as true CCC events, followed by the data augmentation strategy for generating positive training samples. Cell label permutation strategy is applied to generate negative training samples. These samples are mapped to low-dimensional space by a MLP encoder and SupCon loss function is applied to train the network. **c** The applications of scComm in this article: the cell–cell interaction profiling between cell types under various conditions (1), cell clustering using the interaction scores as feature vector (2), and specifically, the identification of the subtypes of neutrophils and tumor cells in the liver cancer study (3, 4)

the respective cell types or custom groups, aligning with traditional interaction analysis methods. The result from contrastive learning determines the significance CCCs between two cell clusters. We also perform statistical tests to determine the statistical

significance of L-R pairs within specific cell clusters. 3) *L-R pair interaction score as cell features:* scComm generates a cell feature matrix where each element of the cell feature vector represents the interaction scores between the specific cell and other cell types on the given L-R pairs. These output options are designed to accommodate diverse analytical needs and to optimize the usability of scComm's interaction scoring system (Fig. 1c).

scComm detects CCCs with high accuracy and sensitivity in simulated data

We evaluated the performance of scComm using simulated datasets, where the background gene expression was sampled from a real cancer dataset (reference dataset) [23]. We then randomly introduced three distinct interaction groups, termed True Positives (TP), each characterized by the varying number of L-R pairs, proportions of cells engaged in interactions, and fold changes in the gene expressions of ligands and receptors (Methods). We validated that the simulated datasets reflected real single-cell data by comparing the distribution of gene expression between simulated datasets and reference dataset (Additional File 1: Fig. S1 and Methods). In our comparative analysis, scComm was evaluated against nine methodologies, including CellChat, CellphoneDB (V3 and V5), NICHES, CellTalker, SingleCellSignalR, Scriabin, ICELLNET, NATMI, and CytoTalk. Given that the majority of these algorithms deduce interactions at the cell type level, we first compared the performance of scComm with other methods at cell-type resolution. We evaluated the proportion of TPs among the top 5 scoring cell-type pairs for each method and scenario. scComm identified the overall highest proportion (87% in average) of TPs, outperforming CellChat (76%), NATMI (60%), NICHES (57%), and CellphoneDB (44%), as illustrated in Fig. 2a. The number of L-R pairs introduced in the communications had little impact on the CCC detection for all methods, as the detecting proportion remained constant across three settings. scComm had a robust performance when the proportion of cells engaged in the CCCs varied, while the performance of CellChat and NICHES was notably diminished under conditions of minimal cell proportion. We noticed that most methods exhibited reduced sensitivity when the L-R gene overexpression level was very low, primarily due to the low signal-to-noise ratio (SNR) (Fig. 2a and Additional File 1: Fig. S2a).

To better mimic real-world complexity, we performed additional simulation study considering unequal numbers of cells across cell types, varying levels of dropout, and mis-annotated cell types (Methods). scComm, CellphoneDB, NATMI, and ICELLNET exhibited stable performance under the varying level of dropout and cell-type misannotation, where the performance of CellChat decreased significantly in noisier situations (Additional File 1: Fig. S2b-d). In the scenario with uneven cell group sizes, scComm and other methods had a reduced performance when reporting CCCs involving larger cell groups. This can be explained by the permutation-based background construction in scComm: when a cell group is large, random label permutations often retain many cells of that group. Consequently, the statistical test becomes more stringent, making it harder for observed scores to reach significance.

We then evaluated the performance of CCC detection at single-cell resolution against two methods, Scriabin and NICHES (cell-to-cell version). In our comparison of the proportion of detected interacting cells among three single-cell resolution methods, scComm consistently detected a greater number of interactions (86% cell pairs in

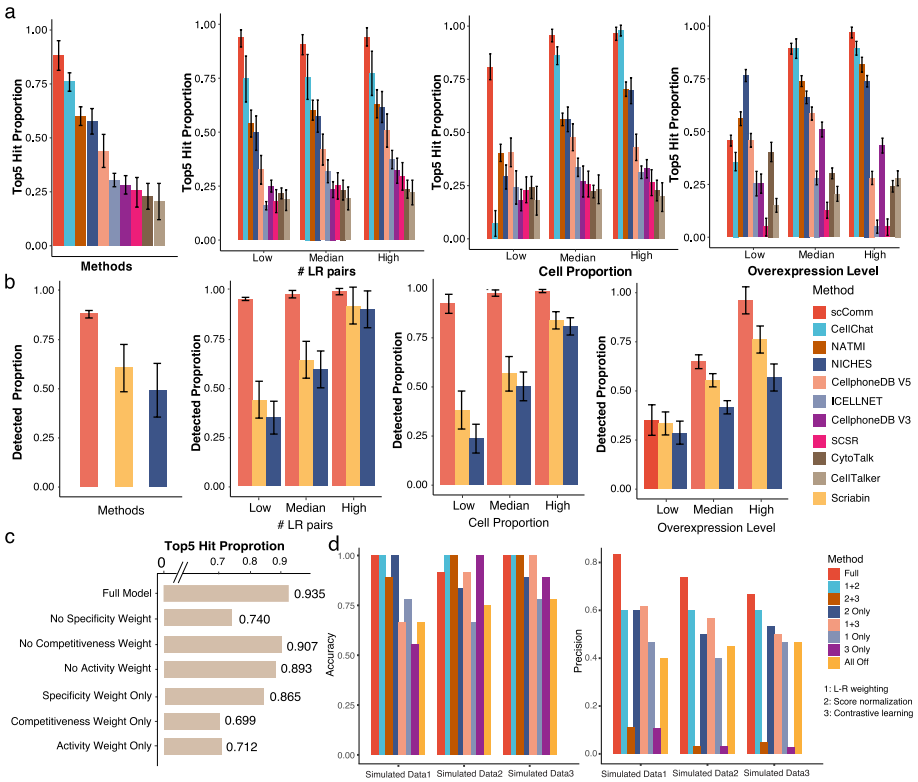

Fig. 2 Performance evaluation on simulated datasets. **a** Comparative analysis of scComm and alternative methods for inferring cell type level communications using simulated datasets ($n = 411$ samples). The left graph depicts the average performance metrics across all scenarios. **b** Evaluation of scComm and other methods for single-cell resolution communication inference on simulated datasets ($n = 91$ samples). The left graph illustrates the average performance metrics across all scenarios, demonstrating scComm's superior detection of interaction pairs and cells. **c** The performance of scComm and its variants on simulated datasets ($n = 96$ samples). The full model of scComm evaluates three weights in the L-R weighting step, thus, six variants (one or two weights are set to 1) were compared to measure the impacts of three weights. **d** The accuracy and precision of scComm in three simulation datasets when turning off some modules. The number in the method name represents the module turned on. 1, 2, and 3 stands for L-R weighting module, score normalization module, and contrastive learning module

average) across all tested scenarios, outperforming Scriabin (59%) and NICHES (49%) (Fig. 2b). scComm had an overall robust performance at different conditions of simulated scenarios, in contrast, the performance of Scriabin and NICHES reduced under challenging conditions of all three scenarios. The study again demonstrated that the superior performance of scComm in discovering the cell pairs involved in CCCs.

In addition, we evaluated the effect of three weights in the L-R weighting step by setting one or more weights to 1 and comparing with the full model. The specificity weight substantially contributed to the detection, resulting in a 18% increase in the detection rate (Fig. 2c). The other two weights also enhanced the results, with a 3% and 4% improvement, respectively. The study proved that the superior performance was attributed to scComm's sophisticated weighting algorithm, especially the measurement of specificity, which ensured reliable results even when faced with variations in the number of L-R pairs or the proportion of interacting cells.

Further, we performed an ablation study to systematically evaluate the contribution of weighting, score normalization, and contrastive learning module. To evaluate the contribution of each component, we conducted a full $2 \times 2 \times 2$ ablation study on the simulation benchmark. In this analysis, each module of scComm was independently disabled as follows: (i) when the weighting scheme was removed, all L-R pairs were assigned weight = 1; (ii) when the geometric scoring module was disabled, we used only the geometric mean of ligand and receptor expression without the normalization step; and (iii) when the contrastive learning was removed, we directly used the raw CCC scores and selected the top 5% as positives, exactly as requested by the reviewer. These three binary choices generated eight model variants covering all possible combinations. The full scComm model overall achieved best performance among its variants, particularly in terms of precision (Fig. 2d). Disabling the weighting or normalization modules led to substantial drops in accuracy, highlighting their essential roles in stabilizing the scoring structure. The contrastive learning module further improved precision by reducing false-positive calls; for example, among the top 5-scoring CCC pairs, two false positives that were included when using raw scores alone were filtered. Together, the ablation study demonstrated the effectiveness of all three modules of scComm, and that the full model is necessary to achieve its best performance.

scComm provides technically reliable outcomes in real-world datasets

To examine scComm's prediction, we sought to demonstrate the biological validity of detected CCCs. We adopted spatial transcriptomic datasets based on the fact that cell pairs with strong interactions are likely to be physically adjacent. We employed scComm on three spatial transcriptomic datasets [24–26], treating the spots as single cells and assigning the cell type of spots using Seurat [27] (Fig. 3a). All three datasets were generated from 10X Visium protocol, with spot size of 55 μm. CCC scores were calculated using contact-dependent L-R pairs annotated in CellChatDB. We observed that the interaction scores between target spot and adjacent spots were elevated compared with distant spots (Fig. 3b). We computed the correlation coefficient between CCC scores and the distance between cell pairs. We observed a negative correlation (the median ranging from -0.3 to -0.05) between CCC scores and the distance for cells with higher interactions in all datasets (Fig. 3c), while this correlation held on only one dataset for cells with lower interactions, potentially due to the low SNR when interaction scores are low. Furthermore, cells predicted to be highly interacting (Top 1% of the interaction score) were found to be in significantly closer proximity compared to distances between random cell pairs (Fig. 3d). The results demonstrated that the interaction scores generated by scComm were supported by spatial proximity of the cells.

We also conducted a performance assessment using real-world datasets [23, 28–30], including two liver cancer datasets, one ovarian cancer dataset, and one pituitary neuroendocrine tumor dataset. In the absence of a definitive gold standard for CCCs in real data, we evaluated the concordance between methods by calculating the correlation of interaction scores between cell types. The CCC scores from scComm, CellChat, NICHES, NATMI, and CellphoneDB exhibited a high degree of correlation, whereas the interaction scores from SingleCellSignalR and CellTalker diverged from the consensus (Additional File 1: Fig. S3).

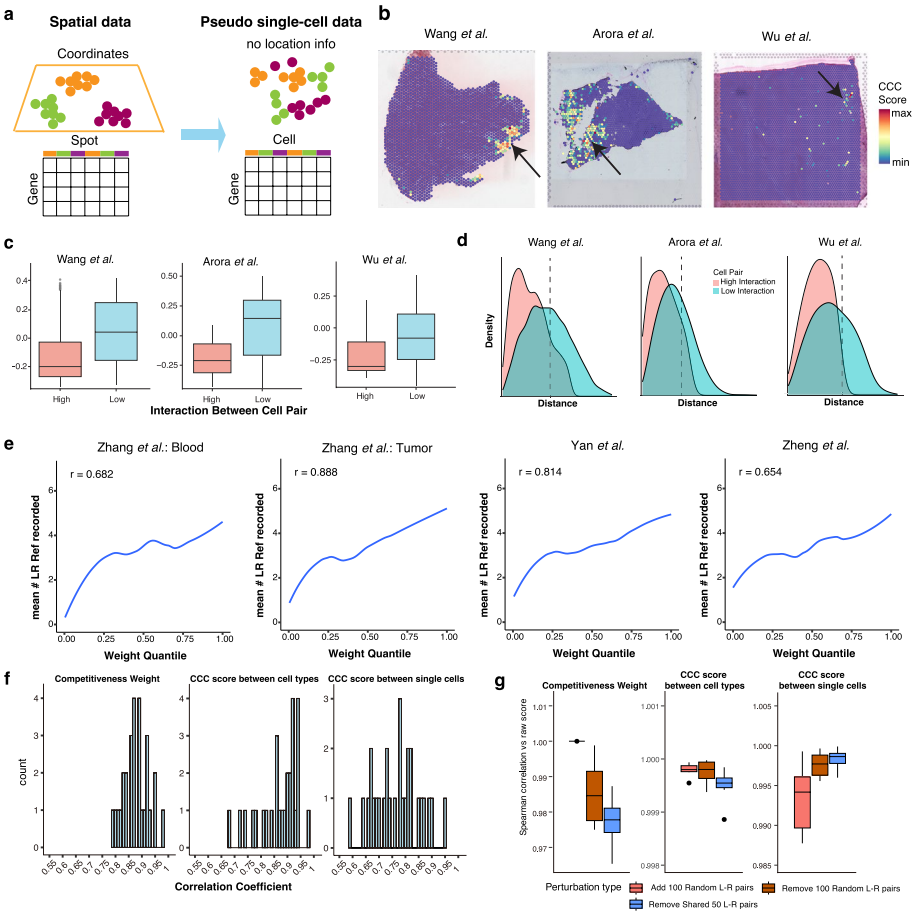

Fig. 3 Technical evaluation on real datasets reveals the reliability of scComm. **a** The description of workflow to validate scComm using spatial transcriptomic datasets. **b** The interaction scores between one spot (marked by an arrow) and other spots. **c** The correlation between CCC scores and cell pair distances in three datasets ($n = 2054, 1185, 4654$ samples). **d** The density plots showing the distribution of cell–cell distances within the top 1% of highly interacting cell–cell pairs predicted by scComm (High Interaction group) and the bottom 50% of interacting cell–cell pairs (Low Interaction group). The vertical dashed lines denote the median distance of all cell–cell pairs in the low interaction group. **e** The number of references in the literature and databases for the L-R pairs against their weights measured by scComm. Pearson's correlations were calculated. **f** The distribution of correlation coefficients of competitiveness weight, CCC score between cell types, and CCC scores between single cells across different L-R databases. **g** The correlation coefficient of competitiveness weight, CCC score between cell types, and CCC scores between single cells between original L-R database and its perturbations using eight L-R databases

We next demonstrated that scComm can reduce the influence of L-R database selection by assigning appropriate weights to L-R pairs. A higher weight assigned to an L-R pair denotes a higher probability and significance in contributing to an intercellular communication event. We observed a good correlation between the weight of L-R pairs and the number of references or databases supporting the L-R pairs, as shown in Fig. 3e. In addition, we applied scComm to a single-cell dataset with eight different L-R databases (OmniPath, CellChatDB, CellPhoneDB, Ramilowski, FANTOM5, ICELLNET, ConnectomeDB2020, and SingleCellSignalR) to evaluate the robustness of CCC predictions. These datasets varied significantly as shown in Additional File 1: Fig. S4a. We observed CCC scores between cell groups or cell pairs had strong pair-wise correlations (median of ~ 0.7–0.85), and competitiveness weight remained consistent across databases

(median correlation of 0.85, Fig. 3f, and Additional File 1: Fig. S4b-e). To further evaluate robustness under noisy conditions, we performed three perturbation experiments: (1) addition of 100 random different artificial L-R pairs for each database, (2) random deletion of 100 true L-R pairs for each database, and (3) deletion of 50 shared pairs across all databases. We observed high pairwise correlations of competitiveness weight and CCC scores between cell groups/cell pairs across these perturbed databases (Additional File 1: Fig. S5a), and these metrics remained highly correlated with the unperturbed results (Fig. 3g and Additional File 1: Fig. S5b, c). The finding suggests that scComm is robust to the selection and variation of L-R databases.

scComm predicts the functional ligand-receptor pairs on the patients with different therapy response in colorectal cancer

Colorectal cancer (CRC) is one of the most common cancer diseases worldwide, characterized by high microenvironmental heterogeneity. Although a wide range of treatment options are available for CRC, clinical outcomes remain highly variable among patients [31]. We apply scComm to a recently published human CRC scRNA-seq dataset [32], which contains 169 samples from 22 patients before and after PD-1 blockade therapy. Patients were categorized into three groups based on their response to therapy: the complete response group (CR), the partial response group (PR), and the steady disease group (SD).

Comparative analysis of computational methods revealed high correlations between scComm, NICHES, CellphoneDB, NATMI, and CellChat results (Fig. 4a). scComm exhibited overall the highest correlation coefficients with other methods. We then compared the changes in score for each L-R pair before and after treatment for each method. scComm exhibited the highest concordance with the consensus (96.5%), following by CellphoneDB (93.7%) and SingleCellSignalR (93.2%) (Fig. 4b). We then designated L-R pairs as the most active L-R pairs if the majority of methods reported their interaction scores ranked within the top 1% of all L-R pairs. Figure 4c shows that over 98% of the most active L-R pairs were ranked within the top 1% by scComm. Additionally, we conducted a pathway-based validation using curated KEGG signaling modules. We selected a signaling pathway and retrieved all L-R pairs known to participate in this pathway, defining them as positives, while all other L-R pairs were treated as negatives. For each algorithm and given cell type-pair, we used the interaction scores to calculate the AUROC (Area under ROC curve). scComm consistently achieved higher AUROC values for biologically relevant receiver cell types (Wilcoxon test, $p < 0.05$) across multiple pathways and treatment stages (Additional File 1: Fig. S6). This result demonstrates that scComm can better captures biologically meaningful signaling patterns, thereby providing functional evidence of validity beyond inter-method agreement.

Next, we assessed the interactions before and after the treatment. The response group, comprising CR and PR, exhibited an overall increase of the number of active L-R pairs after the treatment, while the patients in the SD group had the opposite trend (Fig. 4d and Additional File 2: Table S1). Specifically, CCCs involving T cells, B cells, epithelial cells (including tumor cells), myeloid cells, and stromal cells increased in CR and/or PR patients, while CCCs involving stromal cells and epithelial cells decreased in SD patients (Additional File 1: Fig. S7a). The original study identified

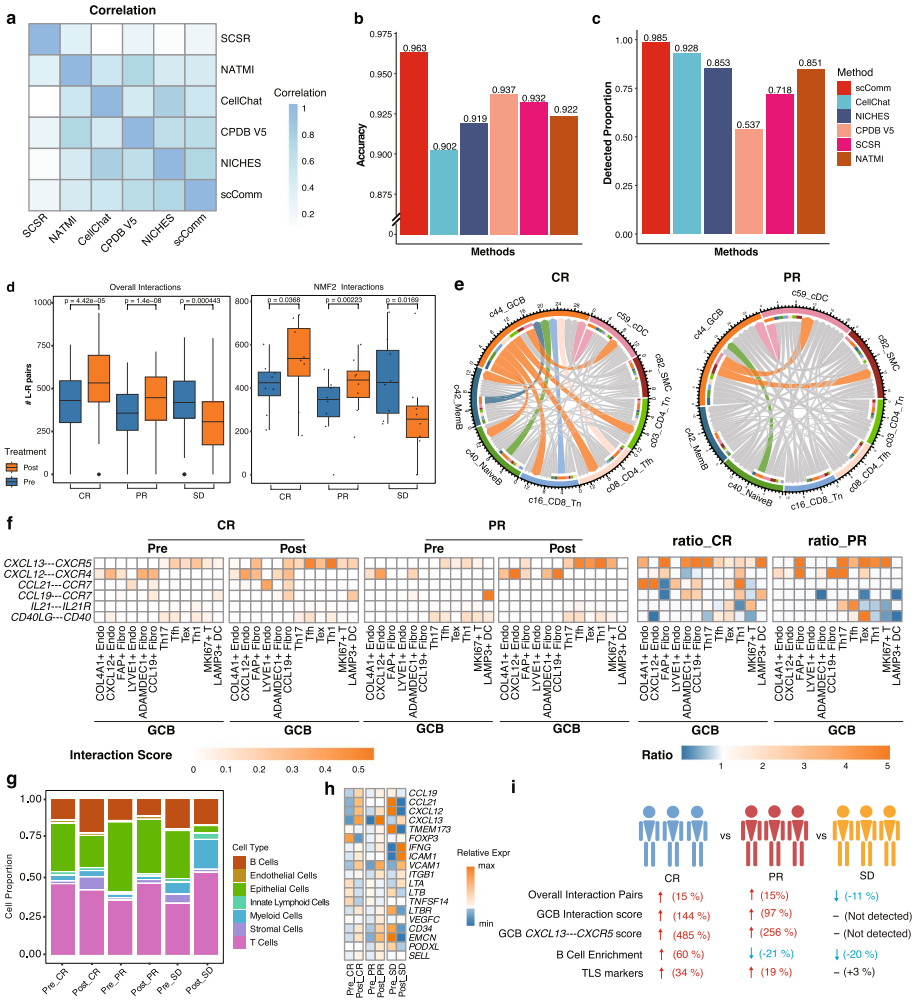

Fig. 4 The cell–cell interaction analysis in colorectal cancer. **a** Pearson's correlation of the CCC scores from scComm and five methods. **b** The proportion of L-R pair score change (increase/decrease) that matched the ground truth reported by each method. The ground truth was determined by the consensus from all methods. **c** The proportion of top 1% L-R pairs recognized by each method. **d** The number of ligand-receptor having positive interaction score between each cell type across all cell types (left, $n = 56$ samples) and NMF2-specific cell types (right, $n = 8$ samples) with all other cell types. The p-values were calculated using a paired two-sided Student's *t*-test. The center line in the boxplot is the median, bounds of boxes are the interquartile of the data, whiskers represent minima/maxima excluding outliers and dots represents outliers of beyond 1.5*Interquartile Range (IQR) from either end of the box. **e** Circos plot shows the interaction scores between two cell types in CR and PR patients. The arrows start from a ligand and end in a receptor. The width of the arrows denotes the ratio of the interaction score after treatment to the interaction score before treatment. Interactions having higher score after the treatment (ratio greater than 2) are showed in color, others are in grey. **f** The heatmap shows the interaction scores between cell types and GCB cells on given L-R pairs. The right two heatmaps indicate the ratio of interaction scores after the before the treatment. **g** The cell proportions in CR, PR, and SD patients before and after treatment. **h** The expression of genes related to TLS formation and maturation. **i** The summary of our analysis for the conclusion that efficacy of PD-1 blockade therapy is directly related to TLS formation. Numbers in the brackets indicate the percentage of change

five cellular programs (NMF1-NMF5) associated with distinct cell type compositions and response patterns. scComm reported the most significant intercellular communication changes before and after the therapy in NMF2 (Fig. 4d and Additional File 1: Fig. S7b), which mainly comprised of components of the tertiary lymphoid structure

(TLS), including T follicular helper-like (Tfh) cells, T helper 1 (Th1) cells, naïve T cells, naïve B cells, and germinal center B (GCB) cells. In patients with colorectal cancer and other types of cancer, the formation of TLS is often associated with improved prognosis [33–37], in which GCB cells play a crucial role in this process [38]. We observed a substantial increase in the intercellular interactions between GCB cells and most cell types in NMF2 after the treatment in CR patients, while this increase was limited to a few cell types in PR patients (Fig. 4e). *CXCL13–-CXCR5* signaling axis was observed in tumor microenvironment (TME) for driving infiltration of B cells but was not elucidated the specific B cell subtypes in the literature [38–40]. Our results demonstrated that GCB cells were the main receiver cells of *CXCL13–-CXCR5* signaling axis (Additional File 1: Fig. S8a). Tfh and Th1 cells exhibited an increased score of *CXCL13–-CXCR5* chemotactic interactions with GCB cells after the treatment in both CR and PR group, which is also consistent with the proportion change of GCB cells after treatment (Fig. 4f, Additional File 1: Fig. S8b, and Additional File 2: Table S2). The interactions with B cells via *CXCL12–-CXCR4*, *CCL21–-CCR7*, and *CCL19–-CCR7* were also reported to facilitate the formation of TLS [41–43], where the sender cells were *CCL19* + fibroblasts and *CXCL12* + endothelial cells, as indicated by our findings (Fig. 4f). Specifically, *CCL21/CCL19–-CCR7* signaling was enhanced significantly in the CR group, providing an explanation of the signal differences in TLS between CR and PR groups, potentially leading to different responses to anti-PD1 therapy. We then evaluated the interaction scores of these chemotactic L-R pairs obtained from existing methods and found that three out of five methods provided results consistent with our findings (Additional File 1: Fig. S8c, 9). In addition to B cell chemotaxis, the infiltration of immune cells and their adhesion to stromal cells also influence TLS formation [33]. We observed the key adhesion molecule *ICAM1–-ITGB2* was significantly activated between stromal cells and epithelial cells in the CR group after treatment (Additional File 1: Fig. S8d). This finding further suggested that the formation of TLS is favorable for enhanced therapy response and improved prognosis. In CR patients, treatment led to an increase in the proportions of B cells and stromal cells, while the proportion of epithelial cells decreased (Fig. 4g).

We examined the transcriptional characteristics of NMF2-associated cell types based on their gene expression signatures based on gene expression signatures (Fig. 4h). The key B cell chemokines such as *CCL19*, *CCL21*, and *CXCL12* were upregulated after treatment in responding patients (CR and PR) but downregulated in stable disease (SD) patients, indicating enhanced B cell and T cell recruitment. *CXCL13* expression increased after treatment across all groups, but the magnitude of upregulation was greater in CR and PR than in SD, indicating stronger B cell-T cell zone formation and tertiary lymphoid structure (TLS) activation in responders. The stimulator of interferon genes *TMEM173*, which is known to enhance antitumor immune responses [44], exhibited distinct expression patterns across patient groups. Its expression showed a modest reduction in CR, a slight increase in PR, and a marked downregulation in SD. *TMEM173* encodes an adaptor protein in the cGAS-STING pathway, which promotes the production of type I interferons (IFN-I) and pro-inflammatory cytokines in response to cytosolic DNA [45]. The suppression in SD suggests the impaired innate immune activation and reduced interferon signaling [46]. We also performed KEGG pathway enrichment

analysis of differentially expressed genes under different treatment conditions and response groups and found that gene highly expressed on CR and PR samples correlated with immune activation, whereas SD samples lacked such enrichment (Additional File 1: Fig. S10).

The upregulation of *IFNG*, a gene associated with T cell function, represented improved T cell activity. The expression of *FOXP3*, a key inhibitory factor in regulatory T (Treg) cells, was downregulated, reflecting a decrease in Treg-mediated immunosuppression. Adhesion molecules such as vascular cell-adhesion molecule 1 (VCAM1), intercellular adhesion molecule 1 (ICAM1), and their receptor ITGB1 were upregulated, facilitating immune cells infiltration into the tumor microenvironment. These gene expression changes are characteristic of mature TLS. On the other hand, in the early stage of TLS formation, lymphoid tissue inducer (LTi) cells interact with stromal cells through lymphotoxin-α1β2 (LTα1β2) binding to the LTβ receptor (LTβR) [47]. The ligands of LTβR including *LTA*, *LTB*, and *LIGHT* (*TNFSF14*) were significantly downregulated. LTα1β2-LTβR signaling pathway leads to the secretion of vascular endothelial growth factor C (VEGFC) by stromal cells and facilitates high endothelial venule (HEV) development [48]. The expression of *VEGFC* remained consistent after the treatment, suggesting that HEV development was not actively occurring. Peripheral node addressin (PNAd), a marker of HEVs composed of GlyCAM-1, *CD34*, Endomucin (*EMCN*), and Podocalyxin (*PODXL*), and essential for immune cell circulation via interaction with L-Selectin (SELL), was upregulated. Together, we concluded that there are more mature and less immature TLS in therapy-responded patients after treatment. These findings suggested that the efficacy of anti-PD-1 therapy in colorectal cancer patients is directly related to TLS formation (Fig. 4i and Additional File 2: Table S3-7). Collectively, these results demonstrate scComm's capacity to uncover correlations between intercellular communications and treatment response, offering the mechanistic insights into PD-1 blockade therapy.

scComm discovers a pro-tumor neutrophil subtype in a liver cancer dataset

Building upon our previous discovery of neutrophil heterogeneity, which reveals unprecedent neutrophil functional diversity in liver cancer according to the gene expression features [28], we applied scComm to further explore neutrophil microenvironment heterogeneity through the CCC patterns. By employing unsupervised clustering using CCC features provided by scComm, we classified neutrophils into two distinct groups (Fig. 5a). Neutrophils in cluster 1 (Neu_1) displayed overall higher CCC scores, including the CCC between neutrophils and tumor cells or endothelial cells (EC), while those in cluster 2 (Neu_2) showed lower CCC scores (Fig. 5b). To validate our findings and compare with other methods, we annotated neutrophils as Neu_1/2 and applied CellChat, CellphoneDB, NICHES, and CellTalker to this dataset. We observed that the outcomes from CellChat, CellphoneDB, and CellTalker supported our conclusion that Neu_1 exhibited increased activity in intercellular communication events (Fig. 5c and Additional File 1: Fig. S11), indicating that scComm can accurately infer the CCC events between single-cell pairs.

Notably, Neu_1 highly expressed *VEGFA* (Fig. 5d and Additional File 1: Fig. S12a, b), which is a key growth factor that stimulates the proliferation and migration of vascular

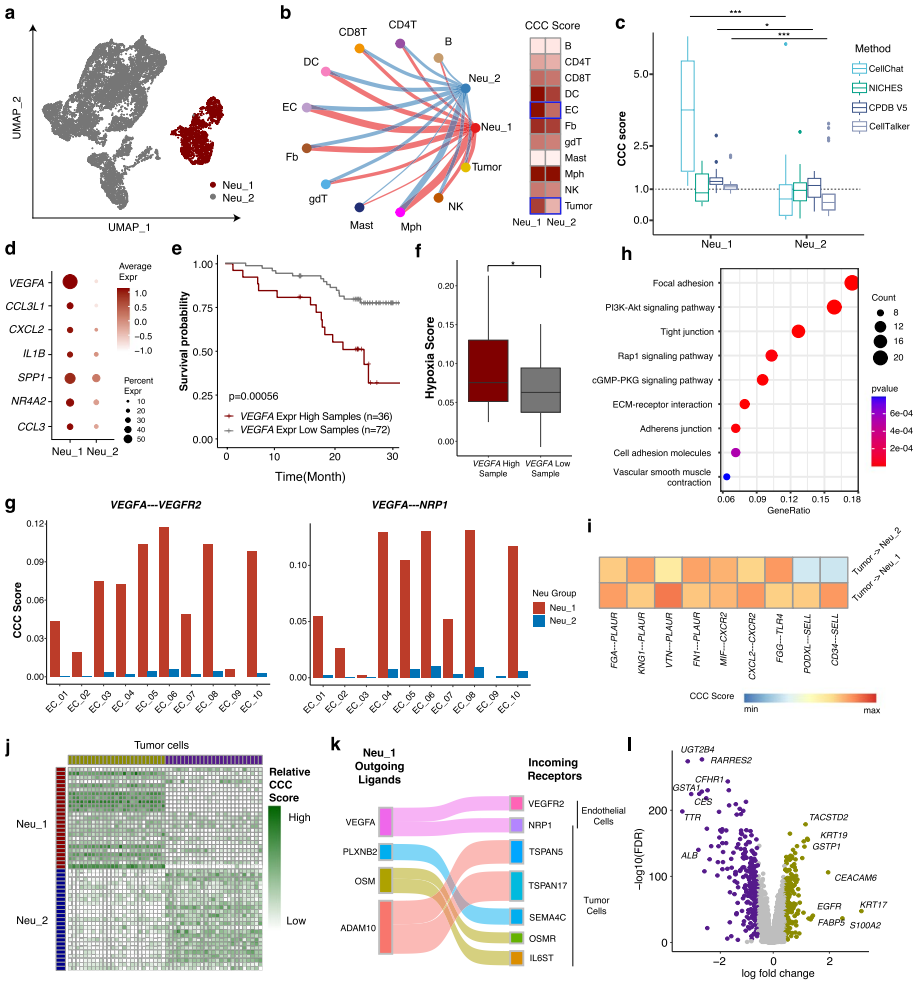

Fig. 5 scComm analysis of neutrophils in a liver cancer dataset. **a** Neutrophils are stratified into two clusters based on their cell–cell communication (CCC) patterns. **b** The CCC scores between Neu_1/2 and other cell populations. The edge width is proportional to the CCC score. **c** The normalized CCC score between Neu_1/2 and other cells obtained from CellChat, CellphoneDB, NICHES, and CellTalker. The scores were normalized against the mean CCC score between Neu_2 and other cell types. **d** The dot plot demonstrates the elevated gene expression in Neu_1. **e** Survival analysis of 108 patients, indicating that increased *VEGFA* expression in neutrophils correlates with poorer patient prognosis. **f** The hypoxia score of *VEGFA* high/low samples. **g** The CCC scores between Neu1/2 and EC subtypes on L-R pairs *VEGFA*–-*VEGFR2* and *VEGFA*–-*NRP1*. **h** The KEGG enrichment analysis of differential expression genes between the EC subtypes EC_04/05/06/08/10 and EC_01/02/03/07/09. **i** CCC scores between tumor cells and Neu_1/2. **j** CCC score heatmap between neutrophils and tumor cells. **k** The outgoing and incoming signaling patterns of Neu_1 and corresponding tumor cells and/or endothelial cells visualized by Sankey plot. The thickness of the flow indicates the CCC score between the L-R pairs. The height of each pattern is proportional to the summed CCC scores. **l** Differential expression analysis in tumor cells divided according to the patterns depicted in Fig. 5j

endothelial cells and is integral to the proliferation and metastasis of solid tumors [49]. When patients were stratified based on the average *VEGFA* expression in neutrophils, higher *VEGFA* expression was correlated with poorer survival outcomes in both this study and the TCGA hepatocellular carcinoma datasets (Fig. 5e and Additional File 1: Fig. S13a, 14a). However, when the patients were stratified based on the proportion of neutrophil subtypes defined in the original paper [28], only the proportion of Neu_10 significantly correlated with the clinical outcomes (Additional File 1: Fig. S13b-h).

Indeed, *VEGFA* is highly expressed in Neu_10, suggesting the coherence of these two variables in survival analysis. In addition, the hypoxia scores of the samples imply that Neu_1 are more likely to be situated in hypoxic tumor microenvironments (Fig. 5f), implying that Neu_1 may play an important role in the tumor progression.

Inspired by the biological function of Neu_1 that highly expressed *VEGFA* and the significant elevated CCC score between neutrophils and ECs, we investigated the intercellular communications between these two cell types. scComm reported significantly higher CCC scores between Neu_1 and ECs compared to those between Neu_2 and ECs, with *VEGFA–-VEGFR2* and *VEGFA–-NRP1* ranking as the top L-R pairs (Fig. 5g). The *VEGFA–-VEGFR2* interaction plays a critical role in regulating angiogenesis, as it is involved in EC proliferation and migration. *NRP1* acts as a co-receptor to *VEGFR2*, which is a primary receptor of *VEGFA* on endothelial cells [50]. This interaction enhances the downstream signaling of *VEGFR2* mediated by *VEGFA* and thereby promotes the blood vessel formation. We observed that EC subtypes 04/05/06/08/10 had higher CCC scores than other EC subtypes. We thereby divided the ECs into the corresponding two subtypes and performed the KEGG enrichment analysis using differential expressed genes (Fig. 5h). Focal adhesions mediate ECs adhesion to the extracellular matrix (ECM), triggering PI3K-Akt signaling to drive EC proliferation, migration, and survival [51]. This integrin-dependent mechanotransduction is further modulated by Rap1 GTPase and cGMP-PKG signaling, which synergizes with VEGF signaling to enhance integrin-mediated ECM adhesion, thereby stabilizing new blood vessels during angiogenesis [52].

The interaction between neutrophils and ECs indicated that Neu_1 reprogrammed the TME with enhanced angiogenesis. We then investigated the intercellular communications between Neu_1 and tumor cells. scComm reported elevated L-R pairs from tumor cells to neutrophils including *CXCL2–-CXCR2*, *MIF–-CXCR2*, and *FGA–-PLAUR*. These interactions facilitated the migration of neutrophils into the tumor microenvironment (TME) (Fig. 5i) [53]. Notably, *PODXL–-SELL* and *CD34–-SELL* were significantly enhanced between tumor cells and Neu_1. *SELL* is a cell adhesion molecule expressed on the surface of neutrophils. Tumor cells recruit neutrophils to the tumor site by binding to L-Selectin (SELL) on neutrophils. We also calculated the CCC scores from neutrophils to single tumor cells and discovered that a subset of tumor cells exhibited elevated CCC scores upon interaction with Neu_1, suggesting a potential role for these neutrophils in tumor reprogramming within specific microenvironments (Fig. 5j). Several well-known L-R pairs were detected between Neu_1 and tumor cells (Fig. 5k). For example, the intercellular communications mediated by *OSM–-OSMR* axis play a crucial role in promoting inflammation and tumor progression. Oncostatin M (OSM), secreted by activated neutrophils, binds to the OSM receptor (OSMR) on tumor cells, triggering signaling pathways that facilitate epithelial-mesenchymal transition and enhance tumor cell survival [54]. *VEGFA–-NRP1* was also reported to promote tumor growth and aggressiveness [55]. Differential expression analysis indicated that tumor cells interacting with Neu_1 tend to be more aggressive and malignant, while genes highly expressed in tumor cells interacting with Neu_2, such as *RARRES2*, *GSTA1*, and *ALB*, may have tumor-suppressive functions [56–58] (Fig. 5l and Additional File 2: Table S8). Recently, Ng et al. used an orthotopic mouse model of pancreatic ductal adenocarcinoma and

identified a terminal neutrophil state, T3, which possesses pro-angiogenic functions and accelerates tumor growth [59]. Over half of the T3 gene markers were found to be highly expressed in Neu_1 (Additional File 1: Fig. S12c, d), corroborating our unsupervised neutrophil clustering based on cell–cell communication and highlighting the consistency with our discovery. In conclusion, our analysis of the CCC revealed that tumor cells recruited neutrophils within the TME, and these neutrophils reprogrammed the TME with enhanced malignancy. Our study not only confirms the neutrophil subgrouping and intercellular communications identified by scComm but also emphasizes the potential of using intercellular communications for cell subtyping.

scComm identifies tumor cell subtypes with distinct intercellular communication patterns and tumor microenvironment

Tumor cells exhibit significant heterogeneity across various physiological features, making it challenging to discern distinct biological characteristics through unsupervised clustering based solely on gene expression. However, leveraging the single-cell resolution capabilities of scComm, we have delineated the interaction patterns of tumor cells in the large liver cancer cohort. We performed hierarchical clustering to the tumor cells using the interaction scores and detected three primary tumor cell groups: one group (tumor type 1, TT1) with heightened interactions with fibroblasts, tumor cells, and endothelial cells; another group (TT2) with increased interactions with T cells and NK cells; and a third group (TT3) primarily interacting with neutrophils (Fig. 6a, b). To validate our clustering results, we manually annotated tumor cells accordingly and employed aggregated methods to assess whether they provided comparable outcomes. All four methods corroborated the strong interactions of all three tumor cell types with their corresponding cell types (Fig. 6c).

The presence of all three tumor cell types in every patient suggested that our clustering captured the intrinsic heterogeneity of the tumor rather than patient-specific variations (Additional File 1: Fig. S15). The varying proportions of these tumor cell types can shape the predominant intercellular communication patterns in patients. We randomly selected three samples, each dominated by the tumor cell type TT1, TT2, and TT3, respectively. Multiplex immunofluorescence (mIF) analysis was conducted on tissue sections to characterize the cellular composition (Fig. 6d, Additional File 1: Fig. S16, and Additional File 2: Table S9). Fibroblasts were colocalized with tumor cells in sample 1, but immune cells were rarely observed, revealing the exclusive cell–cell interactions between fibroblasts and tumor cells. Similarly, T/NK cells and neutrophils were exclusively detected in sample 2 and 3, respectively. The mIF analysis validated the computational inference of CCCs by demonstrating the enrichment of respective cell types in the tumor microenvironment. We further calculated the ratio of TT2 plus TT3 to TT1 in each patient and observed a significant linear correlation between this ratio and the ratio of immune cells to tumor cells in each patient (Fig. 6e), which also highlighted the high level of immune infiltration in TT2/3-enriched patients. Survival analysis and Cox model revealed that TT1 was associated with a poorer prognosis, TT2 was associated with a better prognosis, and TT3 had no significant impact on clinical outcomes (Fig. 6f and Additional File 1: Fig. S17a, b, 14b). We conclude that tumor cells having high interaction with fibroblasts suggests a low-level immune infiltration tumor microenvironment

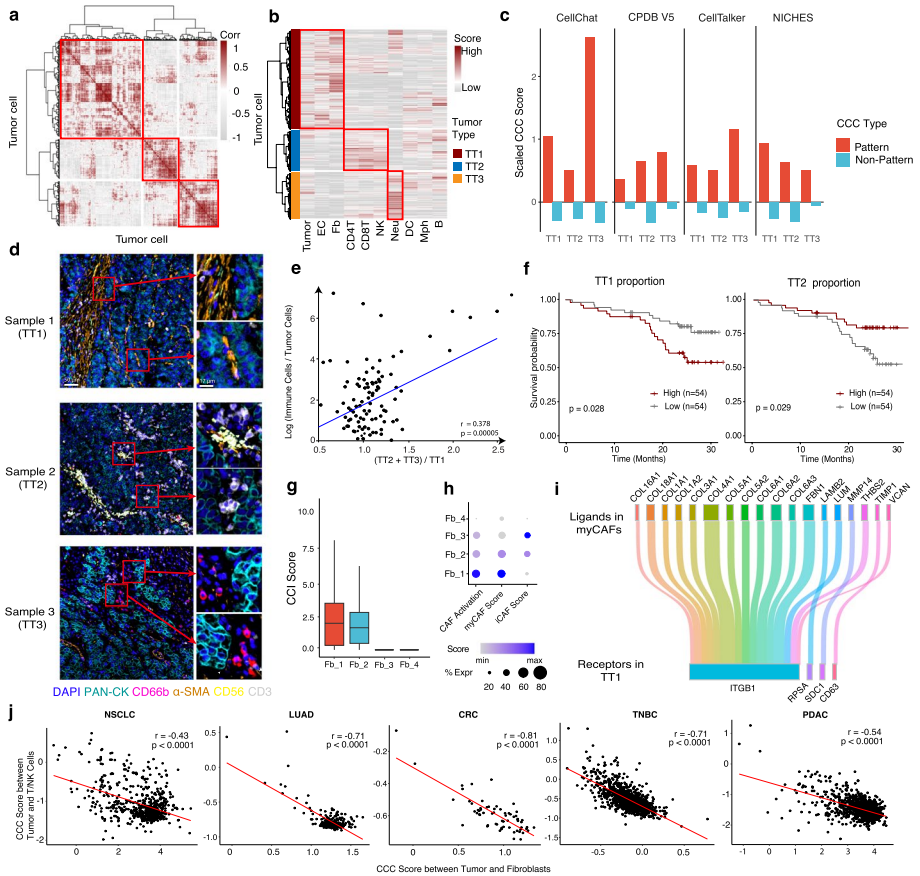

Fig. 6 scComm analysis of tumor cells in a liver cancer dataset. **a** Unsupervised clustering of tumor cells, revealing three subtypes with distinct interaction profiles, identified through Pearson's correlation. **b** Cell–Cell Communication (CCC) scores between individual tumor cells and other cell types, with red boxes indicating significant interaction patterns. **c** CCC scores between TT1/2/3 and other cell types using four existing methods. The red bars (marked as Pattern) indicate the CCC scores between tumor cells and their related receiver cells shown in Fig. 6b, and the blue bars (marked as Non-pattern) indicate the CCC scores between tumor cells and other cells. **d** Immunofluorescence staining of tumor cells (PAN-CK), fibroblasts (α-SMA), T cells (CD3), NK cells (CD56), and neutrophils (CD66b) in tissue sections from three patients, confirming the presence of three interaction pattern types. **e** The correlation between (TT2 + TT3)/TT1 and the proportion of immune cells in each patient. The correlation test was performed using Pearson's correlation and two-sided Student's *t*-test. **f** Survival analysis of 108 patients, stratified by the proportion of Tumor Type 1 (TT1) and TT2. **g** CCC scores between tumor cells and fibroblast subtypes. **h** Score of CAF activation, myCAF, and iCAF in four fibroblasts subtypes. **i** The outgoing and incoming signaling patterns of myCAFs and TT1 cells visualized by Sankey plot. The thickness of the flow indicates the CCC score between the L-R pairs. The width of each pattern is proportional to the summed CCC scores. **j** The CCC scores of tumor cells interacting with fibroblasts and T/NK cells in NSCLC, LUAD, CRC, TNBC, and PDAC dataset. The correlation test was performed using Pearson's correlation and two-sided Student's *t*-test

(TME) and a poorer prognosis. Conversely, tumor cells having high interaction with T cells and NK cells indicates a high-level immune infiltration TME and a better prognosis. The dual role of neutrophils in the early and late stages of tumor development has a complex impact on tumor progression [60], without a significant correlation with prognosis. Differential expression (DE) analysis, however, revealed few DE genes with high fold change among the three tumor cell types, implying that gene expression alone may not be sufficient to distinguish tumor subclusters (Additional File 2: Table S10). Notably, TT1 highly expressed *ITGB1*, a gene encoding a subunit of integrin crucial

for cell-extracellular matrix (ECM) interactions and implicated in tumor progression, metastasis, and therapy resistance [61]. *ITGB1* emerged as a potential prognostic biomarker with a significant p-value in both TCGA hepatocellular carcinoma datasets and this dataset (Additional File 1: Fig. S17c, d).

Consequently, we investigated the mechanism of promoting tumor progression with TT1 by examining the CCCs between fibroblasts and tumor cells, as the interaction scores between fibroblasts and TT1 cells were higher compared to that with endothelial cells (Fig. 6b). We found that myofibroblastic cancer-associated fibroblasts (myCAFs), Fb_1 and part of Fb_2 in the original paper [28], mainly contributed to the interaction with tumor cells (Fig. 6g, h). Figure 6i shows the top-ranked L-R pairs for CCC between myCAFs and TT1, where a majority of the top ligand genes belong to the collagen family. myCAF secreted large amounts of collagens, which are key components of extracellular matrix (ECM). The dense ECM directly impedes immune cells from migrating into the tumor core and promotes cancer growth, thereby resulting in poor survival [62]. CAFs are known to secrete the ECM components that can activate integrin receptors and trigger downstream signaling pathways, such as focal adhesion pathway, PI3K/Akt pathway, and NF-κB pathway, which promote tumor proliferation, anti-apoptosis, cell adhesion, and epithelial-mesenchymal transition [63–65]. The gene set enrichment analysis (GSEA) of the receptor genes in TT1 cell groups showed that the top-ranked receptor genes were enriched in the PI3K/Akt pathway, the ECM-receptor interaction pathway, and the focal adhesion pathway (Additional File 1: Fig. S18a). The upregulated expressions of key genes associated with these pathways validated their involvement (Additional File 1: Fig. S18b). This finding is consistent with the pathways known to be activated by myCAFs, validating the scComm's results.

TT2 showed a distinct characteristic compared to TT1 in this dataset. TT2 had a high immune-infiltration TME that T cells and NK cells provided the cytotoxic effects on the tumors via L-R pairs such as *CADM1--CRTAM* and *TNFSF14--LTBR* [66, 67], as well as the intercellular communication between regulatory/exhausted T cells and tumor cells had the immune inhibitory effects via *CD96*/*TIGIT--NECTIN2* and *AREG--ERBB1*/*EGFR* [68, 69]. To further validate our tumor cell subtype classification, we applied scComm on five public datasets of different cancer types and calculated the intercellular interaction scores between tumor cells and fibroblasts, T cells, and NK cells [32, 70–73]. A negative correlation was observed between the CCC scores of tumor cells--fibroblasts and CCC scores of tumor cells--T/NK cells (Fig. 6j) on all five datasets, indicating that tumor cells strongly interacting with fibroblasts were less likely to interact with immune cells such as T cells and NK cells. This result confirmed that tumor cells interacting with fibroblasts exhibited distinct characteristics such as TME compared to tumor cells interacting with immune cells, which simultaneously emphasized the heterogeneity of tumor cells and the necessity of tumor cell subtyping. This finding further expanded the classification of tumor cell subtypes to encompass a broader spectrum of cancer types.

We additionally run Scriabin and NICHES to perform similar analysis. Scriabin failed to run on this dataset due to extreme memory consumption, while NICHES successfully reported interaction score between single cells and also divided tumor

cells into three clusters (Additional File 1: Fig. S19a). The resulting clusters did not correspond to those identified by scComm (Additional File 1: Fig. S19b). We performed survival analysis and found that the tumor subtypes identified by NICHES did not show any significant survival differences (Additional File 1: Fig. S19c-e). The tumor subtypes identified by scComm show clearer biological interpretability such as intercellular communication patterns and clinical outcomes.

Discussion

In this paper, we present scComm, a computational framework for detecting intercellular communications between single cells. Compare with current methods, scComm has three advantages: (1) It preserves the diversity of signaling behaviors within and between pre-defined cell populations; (2) It aims to report informative CCCs between single cells rather than exhaustively enumerating all possible CCC combinations, improving both analytical precision and interpretability; (3) It enhances the robustness of results across different L-R databases by implementing a data-driven ligand-receptor gene pair scoring module for filtering L-R pairs having minimal impact on CCCs and mitigating database-dependent variability. In the weighting module, scComm assigns high specificity weight to the L-R pairs that activate on specific cell groups and low weight to the L-R genes that are evenly expressed on all cells. scComm also computes the competitiveness and activity weight to quantify the probability of L-R pair involvement in biological processes, thereby minimizing false-positive discoveries. Typically, scComm assigns low weights to the L-R pairs that rarely contribute to CCCs, which are often absent in many databases (Fig. 3e). Thus, the impact of irrelevant L-R pairs is often negligible, rendering the disturbance of the L-R database relatively insignificant. The scoring module of scComm was designed to assign comparable CCC score to each L-R pair on all cell pairs. scComm calculates the z-score of geometric mean of the L-R gene expression and discards all z-scores below zero to eliminate the sequencing noise in scRNA-seq data. Finally, a contrastive learning framework is applied to report significant CCC events. While scComm establishes an optimal balance between analytical comprehensiveness and precision, the framework maintains flexibility through user-adjustable parameters to accommodate specific research requirements.

We assessed the performance of scComm using extensive simulated and real datasets. In the simulation study, we evaluated the accuracy of detected interaction cell types and cells. The superior performance of scComm can be primarily attributed to the weighting module and scoring module, where the weighting module effectively filters out irrelevant L-R pairs and the scoring formula excludes cells with minimal contribution to the interactions. In the real data study, we found that scComm's scoring module provided very consistent results with other methods in different cancer types, including the interaction score between cell type pairs and between ligand and receptor genes. We also applied scComm to a spatial transcriptomics dataset and treated each spot as a single cell. We observed that the interaction scores between spots matched their spatial distances, demonstrating the validity of scComm's method design. However, because each spot may contain mixtures of multiple cell types, assigning a single label via Seurat may raise the risk of artificial interactions or loss of heterogeneity. Although *in-silico* experiment demonstrated that moderate cell mixing does not introduce substantial artificial

interactions (Additional File 1: Fig. S20 and Methods), we do not recommend using scComm on ST datasets.

In the colorectal cancer study, scComm provided the most consistent result with the consensus, suggesting scComm was a reliable tool in analyzing intercellular communications not only between individual cells but also between cell types. For example, scComm detected significant enhancement of CCCs related to the GCB cells after the PD-1 blockade treatment in therapy-sensitive patients. Three existing methods also reported this increasement, strongly supporting our discovery. The limitation of our benchmarking analysis lies in the definition of the ground truth. We used the majority vote among these algorithms as the reference to evaluate prediction accuracy, since we cannot obtain real ground truth on real datasets. While this strategy provides a practical consensus-based comparison, it may introduce bias toward methods that exhibit higher correlations with others (e.g., scComm, CellChat, NICHES, and CellPhoneDB), potentially disadvantaging less correlated algorithms. The reported accuracy and detected proportions should therefore be interpreted with this limitation.

Another important application of scComm, as illustrated in the last two sections, is that interaction patterns can serve to identify cell subpopulations. The interaction patterns, represented by interaction scores between a given cell and all other cells or cell types, provide insights into cellular relationships. CCCs typically occur in the proximity of the given cell, thereby reflecting its local neighborhood structure or microenvironment. Motivated by this, the CCC pattern can serve as a feature of a cell. Cell clustering is typically performed based on the expression levels of known marker genes or overall gene expression similarity. However, in our last two applications, neutrophils and tumor cells were clustered exclusively based on the CCC patterns. Tumor cells were classified into three distinct clusters, each corresponding to a unique tumor microenvironment. Specifically, TT1 cells are characterized by an immune-excluded microenvironment, while TT2 and TT3 cells exhibit a highly immune-infiltrated microenvironment, highlighting the intrinsic differences among these tumor cell subtypes. Thus, CCC patterns can be leveraged for subpopulation identification, which is particularly valuable in tasks such as cell subtype annotation. The ability to distinguish such subpopulations is especially critical in tumor research. Notably, the clustering procedure and criteria employed in this study were not previously reported in any other research.

One limitation of scComm is its higher computational demand compared to current aggregated methods (Additional File 1: Fig. S21). Most cell type-based methods generally required fewer resources, particularly in runtime, compared to single-cell methods. scComm exhibited efficient runtime and moderate memory consumption compared to Scriabin. The higher computational demand of single-cell method is primarily due to its ability to capture within-cell-type heterogeneity, which requires the creation of a data matrix for each individual cell rather than for each cell type. While this increases running time and hard disk usage, it also enables a more granular and biologically relevant analysis. Future optimizations in data storage and computational efficiency may further enhance its scalability. Another limitation is that scComm, like most computational tools for cell–cell communication analysis, relies on existing L-R databases. It evaluates the weight and significance of L-R pairs within these databases and assigns interaction patterns accordingly. While novel L-R pairs need to be integrated into the

database manually before running scComm, this design ensures compatibility with curated resources and offers flexibility for users to incorporate emerging discoveries. Future updates may streamline this process to facilitate the incorporation of novel interactions more seamlessly.

Recent technological advances in spatial transcriptomics (ST) have enabled simultaneous measurement of gene expression profiles and spatial cellular relationships [74]. This approach significantly improves the accuracy of analyzing CCCs by considering the distance of interacting cells, as interacting cells typically maintain proximity within 10–20 cell diameters [75, 76]. Consequently, detecting CCCs using ST data eliminates the occurrence of false positive interactions, which arise between cells that are excessively distant. The scComm framework can be readily modified to accommodate ST data by incorporating the distance between cells as an additional weighting coefficient and designing appropriate hypothesis testing procedures.

Overall, our results strongly validated that scComm is a powerful tool for deciphering CCCs at single-cell resolution. We are confident that scComm will play a pivotal role in unraveling the intricate patterns of single-cell interactions. We anticipate that scComm will find extensive applications in single-cell tumor research, thereby advancing the frontiers of intercellular communication research.

Conclusions

In this study, we present scComm, a bottom-up computational framework for inferring cell–cell communication at single-cell resolution. By integrating a data-adaptive ligand-receptor weighting strategy with supervised contrastive learning, scComm effectively selects biologically meaningful interactions, filters noise, and circumvents the limitations of prior clustering. Our benchmarking demonstrates superior accuracy and sensitivity compared to existing approaches, enabling the detection of communication events involving rare or functionally distinct cell populations. Applications to colorectal and liver cancer datasets reveal new insights into tumor-immune interactions, angiogenesis, and microenvironmental heterogeneity, highlighting scComm's utility in both mechanistic discovery and biomarker identification. We anticipate that scComm will serve as a versatile tool for dissecting intercellular communication across diverse biological contexts, ultimately advancing our understanding of complex cellular ecosystems and informing therapeutic strategies.

Methods

Data preparation

The scComm framework requires three inputs: a single-cell gene expression matrix with corresponding cell annotations; the OmniPath L-R database, which can be supplemented with custom L-R pair lists to accommodate specific research objectives; and the DoRothEA database [77] or custom database, serving as a repository for transcription factor (TF) regulatory data.

Data-adaptive learning module for weighting L-R pairs

The weight of each L-R pair in each cell group pair is calculated by multiplying three separate weights w_1, w_2, w_3 learned from the gene expression in the related cell groups.

w_1 evaluates the L-R specificity in each cell group pair formularized by term frequency-inverse document frequency (TF-IDF) method. The specificity of ligand-receptor (L-R) pairs is evaluated to discern those exhibiting significantly higher expression levels within a restricted subset of cell group pairs. This subset is hypothesized to represent a population of interest that may hold significant research value. The term frequency (TF) of a gene in cell group j is defined as:

$$\mathrm{TF}(\mathrm{gene}) = \frac{x_{\mathrm{gene},j}}{X_j},$$

where $x_{\mathrm{gene},j}$ is the mean expression of the gene in cell group j, and X_j is the sum of $x_{\mathrm{gene},j}$ for all genes in cell group j. We define inverse document frequency (IDF) of a gene in cell group j as:

$$\mathrm{IDF}(\mathrm{gene}) = -\log\frac{x_{\mathrm{gene},j}}{X_{\mathrm{gene}}},$$

where X_{gene} is the sum of $x_{\mathrm{gene},j}$ for all cell groups. Here, IDF is equivalent to the self-information of a variable in information theory.

The specificity is quantified through the calculation of TF-IDF weight for each ligand and receptor gene, defined as:

$$H(\mathrm{gene}, j) = -\frac{x_{\mathrm{gene},j}}{X_j}\log\frac{x_{\mathrm{gene},j}}{X_{\mathrm{gene}}}.$$

The first weight w_1 of a given L-R pair between cell group j_1 and j_2 is then given by:

$$w_1(\mathrm{L}-\mathrm{R}, j_1, j_2) = H(\mathrm{L}, j_1) * H(\mathrm{R}, j_2).$$

In other words, we prioritize L-R pairs in which both ligand and receptor genes are cell group-specific. To facilitate the comparative study, we scale w_1 to obtain the same median (0.5 by default) across all datasets.

Subsequently, we determine the competitive potential w_2 for each ligand and receptor pair. In the case a receptor gene is targeted by multiple ligands, we posit that ligands exhibiting higher expression levels are more likely to engage with the receptor, thereby facilitating cell signaling pathways. Given a receptor R, the activity score of its ligand l_i for cell group j_1 is defined as:

$$a_{i,\mathrm{R},j_1} = \frac{e^{\eta x_{l_i,j_1}} - 1}{e^{\eta \max_m x_{l_m,j_1}} - 1},$$

and conversely, given a ligand L, the activity score of its receptor r_i for cell group j_2 is:

$$a_{i,\mathrm{L},j_2} = \frac{e^{\eta x_{r_i,j_2}} - 1}{e^{\eta \max_m x_{r_m,j_2}} - 1},$$

where η is a tuning parameter (0.1 by default). The activity score quantifies the ligand/receptor's relative expression level in comparison to the expression levels of its competitive counterparts within the cellular context. Either high $a_{\mathrm{L,R},j_1}$ or $a_{\mathrm{R,L},j_2}$ can yield high competitive potential, so we define the second weight of a given L-R pair as the square root of normalized sum of squares of $a_{\mathrm{L,R},j_1}$ and $a_{\mathrm{R,L},j_2}$:

$$w_2\left(\mathrm{L}-\mathrm{R},j_1,j_2\right)=\sqrt{\frac{a_{\mathrm{L,R},j_1}^2+a_{\mathrm{R,L},j_2}^2}{2}}.$$

In the subsequent step, we assign scores to the L-R pairs based on the regulatory impact of their associated TFs. The hypothesis is that the activation of cellular communication through an L-R pair is modulated by the activity of the corresponding TFs. To quantify this, we calculate the correlation coefficients between the expression levels of a gene and those of its regulatory TFs within each cell group, employing this metric to refine the scoring of L-R pair interactions.

$$r_{\mathrm{gene},j}=\frac{1}{l}\sum_{g}\left|\mathrm{cor}\left(x_{\mathrm{gene},j},x_{g,j}\right)\right|,$$

where g represents the TFs of the given gene in the database, l is the number of TFs of the given gene. The third weight is calculated as:

$$w_3\left(\mathrm{L}-\mathrm{R},j_1,j_2\right)=\mathrm{sigmoid}\left(\frac{r_{\mathrm{L},j_1}+r_{\mathrm{R},j_2}}{2},\lambda\right),$$

where λ is the scaling parameter of the sigmoid function (3 by default), and the sigmoid function is defined as:

$$\mathrm{sigmoid}(x,\lambda)=\frac{1}{1+e^{-\lambda x}}.$$

Finally, the weight of a given L-R pair in cell group j_1 and j_2 is:

$$w\left(\mathrm{L}-\mathrm{R},j_1,j_2\right)=w_1\left(\mathrm{L}-\mathrm{R},j_1,j_2\right)*w_2\left(\mathrm{L}-\mathrm{R},j_1,j_2\right)*w_3\left(\mathrm{L}-\mathrm{R},j_1,j_2\right).$$

Scoring the interaction of each cell pair on each L-R pair

For each ligand-receptor (L-R) pair, we define the raw interaction score $s_{ij}^{\mathrm{L-R}}$ between cell i and j by employing the geometric mean of the ligand and receptor gene expression values:

$$s_{ij}^{\mathrm{L-R}}=\sqrt{x_{\mathrm{L},i}x_{\mathrm{R},j}}.$$

This geometric mean is then normalized across all cell pairs:

$$\widehat{s}_{ij}^{\mathrm{L-R}}=\frac{\left(s_{ij}^{\mathrm{L-R}}-\bar{s}^{\mathrm{L-R}}\right)}{\sigma^{\mathrm{L-R}}},$$

where $\bar{s}^{\mathrm{L-R}}$ and $\sigma^{\mathrm{L-R}}$ is the average and standard deviation of $s_{ij}^{\mathrm{L-R}}$ among all cell pairs, respectively. Here, the geometric mean mitigates the influence of disproportionately high gene expression levels. This normalization step ensures comparability across genes. We then scaled $\hat{s}_{ij}^{\mathrm{L-R}}$ by the pre-calculated weight of the respective L-R pair:

$$M_{\mathrm{L-R},i,j} = \hat{s}_{ij}^{\mathrm{L-R}} * w\left(\mathrm{L-R}, c_i, c_j\right),$$

where c_i and c_j is the cell type of cell i and j, respectively.

This normalization step ensures comparability across genes. The rationale for this method is that the significance of each L-R pair has been previously established through the weighting process. We drop the negative values after normalization, mimicking the dropout procedure in the network inference algorithm [78]. Additionally, we cap all values at a threshold (5 by default) to mitigate the influence of exceptionally high-expressing genes. The resultant cell–cell interaction tensor, denoted as M, encapsulates the interaction scores for each cell pair across all L-R pairs, thus preparing it for subsequent analytical processes.

The contrastive learning model

To identify biologically informative CCC events from background noise, we design a contrastive learning framework. The model input consists of L-R pair score vectors for each pair of cell groups, computed as the mean score between all cell pairs from the two cell groups. We designate cell group pairs within the top 5% of total L-R pair scores as positive samples and denote the corresponding feature matrix as Y_{P1}, as we found that the results were highly stable within the range of 2% to 10%, where the number of significant interacting pairs showed negligible changes. Given the limited number of positive samples, we implement a data augmentation strategy to generate more positive samples for contrastive learning. Specifically, for each original interaction feature vector representing a cell group pair, a 10% random dropout perturbation is applied to preserve the overall intrinsic communication signals while introducing minor variations, thereby generating augmented positive samples. The feature matrix of these augmented samples is denoted as Y_{P2}. These two matrices are concatenated to form the combined feature matrix $Y_{\mathrm{P}} = [Y_{\mathrm{P1}}, Y_{\mathrm{P2}}] \in \mathbb{R}^{r_1 * n}$, where r_1 represents the number of positive samples and n represents the number of L-R pairs.

For negative samples, we adopt a cell label permutation strategy to construct cell group pairs that are unlikely to engage in CCC events. Specifically, L-R pair score matrices $Y_{\mathrm{N}}^{(b)} (b = 1, \ldots, B)$ are computed for the b-th shuffled cell groups and concatenated into $Y_{\mathrm{N}} = \left[Y_{\mathrm{N}}^{(1)}, Y_{\mathrm{N}}^{(2)}, \ldots, Y_{\mathrm{N}}^{(B)}\right] \in \mathbb{R}^{r_2 * n}$, where r_2 represents the number of negative samples. Subsequently, a two-layer fully connected network is employed to project each cell group pair's feature vector into a 64-dimensional embedding space. The model is trained by minimizing the SupCon loss function and optimized with the Adam optimizer. Here, the SupCon loss function is:

$$L = -\frac{1}{r_1 + r_2} \sum_i \frac{1}{|P(i)|} \sum_{p \in P(i)} \log \frac{\exp(\mathrm{sim}\left(z_i, z_p\right)/\tau)}{\sum_{a \in A(i)} \exp(\mathrm{sim}(z_i, z_a)/\tau)},$$

where i indicates any positive/negative sample, z_i is the low-dimensional embedding of sample$i$, $P(i)$ represents the samples having the sample label as sample$i$, $A(i)$ represents all samples except sample$i$, sim(,) is the cosine similarity function, and τ is the temperature parameter (0.5 by default).

After training the encoder network with the supervised contrastive learning framework, we applied the trained encoder to the full dataset to obtain low-dimensional feature representations. These feature vectors were then used as input for a logistic regression classifier, which had been trained on the feature embeddings from the labeled positive and negative datasets.

Downstream analysis utilizing cell–cell interaction scores

The cell–cell interaction score tensor M can be transformed into a feature-by-cell matrix F, where each cell's feature vector comprises its interaction scores with all other cell types by calculating the mean interaction score of the cells in the same cell type. This matrix can be used for various downstream analyses, including dimensionality reduction, clustering, and the identification of neighboring cells. Researchers are empowered to define interaction patterns, or custom cell groups, aligned with their specific analytical objectives, and aggregate cells accordingly to discern these patterns.

Furthermore, to facilitate comparisons with traditional analysis methods, scComm allows for the aggregation of cells into predefined cell types, creating a cell type-by-cell type interaction score matrix. This traditional format mirrors the outputs generated by established tools such as CellChat and CellphoneDB, where matrix entries represent the averaged interaction scores between all cells of each respective type. This approach not only enhances the interpretability of the data but also enables integration with existing analytical workflows and methodologies.

Statistical analysis for L-R pair interaction significance under different conditions

scComm facilitates the quantification of cell–cell interactions across single or multiple samples. In experiments with biological replicates, it is essential to statistically assess whether the interaction strength of a given L-R pair between two cell groups differs significantly across conditions. To achieve this, for each L-R pair and each pair of cell groups, a two-sided Student's t-test is then performed across replicates to test for differences in interaction strength between conditions. This design ensures that the test is based on independent observations at the replicate level, thereby satisfying the assumptions of the t-test. Multiple testing is accounted for using the Benjamini-Hochberg (BH) procedure, and L-R pairs with a q-value below 0.05 (by default) are considered to exhibit significant interaction differences and are retained for further analysis.

Statistical analysis L-R pairs between two cell groups

To ascertain the statistical significance of interaction scores for L-R pairs, we employ permutation tests. scComm generates a null distribution of interaction scores by randomly permuting the cell annotation labels, which allows us to assess the interaction

scores for L-R pairs between any two groups under the null hypothesis of no biological interaction. We define matrix C is a cell type-by-cell type interaction score matrix for one given L-R pair, we calculate $C_{ij}^{(b)}(b = 1, \ldots, B)$ for b-th shuffled cell group i and j, and denote ν and σ^2 be the mean and variance of $C_{ij}^{(b)}$, respectively. The distribution of $C_{ij}^{(b)}$ can be approximated by a normal distribution with these mean and variance values (Additional File 1: Fig. S22a). Here, the permutation procedure is used for null parameter estimation. The p-value for the interaction score between group i and j is calculated as $p_{ij} = 1 - \Phi\left(\frac{C_{ij}-\nu}{\sigma}\right)$, where Φ is the cumulative distribution function of the standard normal distribution, followed by BH FDR correction. We set $B = 100$ by default, as we have tested that $B = 100$ and $B = 1000$ yield very similar results (Additional File 1: Fig. S22b, c).

Simulation setup

For the generation of simulation data, we utilized background expression patterns derived from real datasets. Our approach involved the alteration of gene expression profiles to incorporate random cell–cell interaction patterns. Specifically, we calculate the average expression and the variance of each gene for each cell type defined in the original study, denoted as ν_{gj} and σ_{gj}^2 for gene g and cell group j. GENIE3 was applied to analyze the gene regulatory network and the top 10% of the regulatory link will be reported [79]. We calculated Pearson's correlation between source genes and target genes reported from GENIE3 to form the correlation matrix P. Note that the correlation of an unreported gene pair is set to 0, and the diagonal of P is also set to 0. For each cell type, we simulated the gene expression of 200 cells following the negative binomial distribution with the mean and variance from the background expression. We set the number of cell types to ten and obtain an expression matrix containing 2,000 cells denoted as $X\prime$. Within each simulation dataset, we integrated three distinct cell–cell interaction patterns. Each pattern involved the random selection of two cell groups, designated as the sender and receptor, respectively. We randomly selected three to ten ligand-receptor (L-R) pairs from the same biological pathway, ensuring a biologically plausible interaction. The selection of L-R pairs and their pathways was facilitated by the CellChat database. For the cells implicated in these interactions, we randomly selected 20%−100% of cells in those groups and adjusted the expression levels of the corresponding ligand and receptor genes. We set the selected ligand and receptor gene expression in the selected cells by resampling from the negative binomial distribution with mean $r\nu_{gj}$ and variance $r\sigma_{gj}^2$ to generate the gene expression matrix $X\prime\prime$, where r is the overexpression ratio ranging from 1.5 to 50. We adjust the expression using the gene correlation we learned and obtain the final gene expression matrix

$$X = X'' + P^T(X'' - X\prime).$$

To evaluate methods in more challenging conditions, we performed additional simulation study considering unequal numbers of cells across cell types, varying levels of dropout, and mis-annotated cell types. Specifically, we simulated ten datasets for each of the scenario: (1) unequal numbers of cells across interacting cell types (with one cell group containing 30% of total cells, one with 20%, one with 15%, and seven smaller groups

containing 5% each), (2) varying dropout rates (ranging from 3%−30%), and (3) cell-type misannotation (3–30% random label perturbation).

In our simulation study, we embedded three distinct interaction patterns within each dataset to assess the capability of various methods in scoring cell-group interactions. We categorized cell proportions into low ($\leq$20%), median (30%−50%), and high ($\geq$60%) to reflect varying degrees of interaction participation. Similarly, the number of L-R pairs was classified as low (3 or 4), median (5 or 6), and high (7 or more) to indicate the complexity of interactions. Overexpression levels were also stratified into low (fold change < 5), median (fold change 8–20), and high (fold change > 20) to account for differential gene expression intensities. The dropout rate was divided into three groups: Low (3%−9%), Median (12%−21%), and High (24%−30%). The misannotation rate was divided into three groups: Low (3%−9%), Median (12%−21%), and High (24%−30%). The overexpression level in the additional simulation study was divided into three groups: Low ($1.5\times-2\times$), Median ($2\times-3\times$), and High ($3\times-4\times$).

For single-cell resolution performance comparison, we initially calculated the proportion of interacting cell pairs, denoted as p. For instance, if 70% of cells from one type were set to interact with 70% of cells from another, this results in 70%*70% = 49%, or 49% of cell pairs being involved in the interaction. We then calculated the p-th quantile of the interaction scores for all cell pairs between two specified cell types, using this value as the threshold t. The detected proportion, representing the fraction of cell pairs with scores surpassing t, served as a metric for evaluating the methods' efficacy in discerning interactive from non-interactive cell pairs.

To assess whether our simulation datasets mimic real single-cell data, we compared key summary statistics, including gene expression mean, gene expression standard variation, and zero proportion, between the simulated datasets and reference (Additional File 1: Fig. S1a-c). We also performed Kolmogorov–Smirnov (K-S) test, showing no significant distributional differences between the simulated and reference data (Additional File 1: Fig. S1d-e). Moreover, dimensionality reduction analysis revealed that simulated and real cells were fully mixed (Additional File 1: Fig. S1f), further supporting that the simulation captures the distributional characteristics of real single-cell data.

Cell–cell interaction analysis

We apply scComm to the single-cell RNA-seq gene expression data of each patient. To compare with traditional cell type-level methods, the cell type-level interaction score matrix C is used to measure the interaction.

In the colorectal cancer dataset, a total of 56 cell types were included as the complete set of NMF cell types, with subsets further categorized as NMF1-5 cell types. For each cell type, we calculated the number of potential LR pairs capable of interacting with all other cell types. To investigate whether differences in cell type ratios influence cell–cell interactions, we calculated the ratio of each cell subtype within its corresponding major cell type across all samples under pre-treatment (baseline) and post-treatment conditions. To evaluate changes in cell–cell interaction dynamics associated with anti-PD1 therapy, we analyzed interaction scores under these two conditions. Interaction scores were calculated for all sub-cell type pairs. Results were further stratified by clinical

response categories, including complete response (CR), partial response (PR), and stable disease (SD).

In the neutrophil analysis, we calculate the interaction score between each neutrophil and tumor cells for each L-R pair and obtain a matrix of interaction scores, where the entries are the average of CCC scores on one L-R pair between one neutrophil and all other cells. We retain the top 400 high-variation interactions and then perform dimension reduction and clustering using this matrix to detect the cell groups with high/low interaction.

In the tumor cell subtyping analysis, we retain the top 20% high-variation interactions to evaluate the mean interaction scores between cells of different cell types and the given tumor cell. These are the feature vectors for hierarchical clustering and correlation coefficient calculation.

For five validation datasets in tumor cell subtyping analysis, we first annotated cells using SingleR (v1.10.0) and calculated the interaction scores between each epithelial cell and other cells. We then aggregated the fibroblasts, T cells, and NK cells to obtain an average interaction scores between each epithelial cell and fibroblasts or T/NK cell types.

CellphoneDB (v5.0 and v3.0), CellChat (v2.0.0), NICHES (v1.0.0), SingleCellSignalR (v1.8.0), CellTalker (v 0.0.7.9000), NATMI, ICELLNET (v1.3.0), Cytotalk (v0.99.0), and Scriabin (v 0.0.0.9000) were all run using their default parameters with the same L-R database. The cell–cell interaction scores of CellChat, CellTalker, SingleCellSignalR, and NICHES are obtained from res@net$weight, res$interact_ratio, res$`individual-networks`[[GroupName]]$LRscore, and res$CellToCell@assays$CellToCell@counts, respectively. CellphoneDB reports the interaction scores in the file 'simple_analysis_interaction_scores.txt' for V5 and 'mean.txt' for V3. Scriabin returns a Seurat object that contains the interaction score matrix with rows for L-R pairs and columns for cell pairs, stored in the variable res@assays$CCIM@data. ICELLNET returns interaction score for each cell type, and we manually merged them into an interaction matrix. CytoTalk detected CCCs once for a given cell type-pair, and the CCC scores for each cell type-pair were obtained from sum(result$pathways$df_pval $potential). NATMI reports CCC scores for each L-R pair and each cell type-pair, so we calculated the sum of CCC scores for all L-R pairs for a given cell type-pair stores in 'Edges_lrc2p.csv'.

Gene expression analysis

We used Seurat (v 4.3.0.1) to read the gene expression count matrix. The expression was further normalized using the NormalizeData function in Seurat. Highly variable genes were identified using the FindVariableGenes function. Their expression was scaled and centered along each gene using the ScaleData function. We then performed dimension reduction using principal component (PC) analysis. We selected the first 20 PCs for Uniform Manifold Approximation and Projection (UMAP), and UMAP plots were generated using the DimPlot function in Seurat. To identify differentially expressed genes, we used the FindAllMarkers function in Seurat with Wilcoxon's rank-sum test. Genes expressed in at least 10% of cells within a cluster and with an adjusted p-value smaller than 0.05 were considered differentially expressed. GENIE3 (v 1.18.0) was run under its default parameters to infer the gene regulatory network.

In-silico experiment for estimating the aggregation error in ST datasets

We used a public scRNA-seq dataset with cell-type annotations, and we randomly merged K (K = 4, 8, and 10) single cells into pseudo-bulk cells to mimic the case where one spot contains multiple cells. We ran scComm on both the original and aggregated datasets, and the CCC intensity scores from the original dataset were merged accordingly for comparison. The correlation coefficients between the two CCC intensity vectors were then calculated.

Multiplex Immunofluorescence (mIF), tissue imaging, and analysis

All the Formalin-fixed and paraffin-embedded (FFPE) tissues used within the experimental operation were sectioned as slides of 2–5 μm thickness. The slides were deparaffinized in xylene for 30 min and rehydrated in absolute ethyl alcohol for 5 min (twice), 95% ethyl alcohol for 5 min, and 75% ethyl alcohol for 2 min sequentially. Wash the slides with distilled water 3 times. A microwave oven is used for heat-induced epitope retrieval, and during epitope retrieval, the slides were immersed in boiling EDTA buffer (ZLI-9079, zsbio, Beijing, China) for 15 min. Antibody Diluent/Block from Alpha X Bio was used for blocking. The mIF experiments were performed by AlphaXPainter X30 (Alpha X Bio, Beijing, China) in which primary antibodies were used as listed in below: rabbit anti-human CD66b, Abcam (ab197678), 1:100; rabbit anti-human α-SMA, Abcam (ab124964), 1:4000; mouse anti-human CD56, ZSGB-Bio (ZM0057), 1:100; mouse anti-human CD3, Alphaxbio working solution; mouse anti-human PANCK, Alphaxbio working solution. All the primary antibodies were incubated for 1 h at 37 °C. Then slides were incubated with Alpha X Ploymer HRP Ms + Rb (Alpha X Bio, Beijing, China) for 10 min at 37 °C. Alpha X 7-Color IHC Kit (AXT37100031, Alpha X Bio, Beijing, China) was used for visualization. After each staining cycle, heat-induced epitope retrieval was performed to remove all the antibodies including primary & secondary antibodies. The slides were counter-stained with DAPI for 5 min and enclosed in Antifade Mounting Medium (I0052; NobleRyder, Beijing, China). Images were scanned with ZEISS AXIOSCAN 7 (ZEISS, Oberkochen, Germany). Images were analyzed with HALO software (v3.6; Indica Labs, USA).

Supplementary Information

The online version contains supplementary material available at https://doi.org/10.1186/s13059-026-04043-9.

Additional file 1. Supplementary figures. Figure S1-22.

Additional file 2. Supplementary tables. Table S1-10.

Acknowledgements

We thank Wenjie Sun for the suggestions in the benchmarking and Qi Cao for the suggestions in data analysis. We are grateful to Alpha X Biotech (Beijing) Co., Ltd for excellent technical assistance and support in mIF design.

Peer review information

Mingyao Li and Wenjing She were the primary editors of this article and managed its editorial process and peer review in collaboration with the rest of the editorial team. The peer-review history is available in the online version of this article.

Authors' contributions

N.Z., Z.X., Z.J., Z.T., and X.L. conceived the study. Z.J., Z.T., and K.Z. designed the experiments. Z.J., Z.T., and X.L. developed the computational method and performed data analysis. N.Z., Z.J., Z.T., X.L., and Z.X. wrote the manuscript. N.Z. supervised the work. All authors read and approved the final manuscript.

Funding
This work was supported by the National Natural Science Foundation of China (82588201 and 82341005 to N.Z. and 32400510 to Z.J.), the National Science and Technology Major Project of China (2022YFC3400900 to N.Z.), the China Postdoctoral Science Foundation (2022M720308 to Z.J.), and the Beijing Natural Science Foundation (5244030 to Z.J. and QY23058 to X.L.).

Data availability
scComm is available on GitHub (https:/github.com/ZijieJin/scComm) [80] and Zenodo (https://doi.org/10.5281/zenodo.18946992) [81] under MIT license. The scRNA-seq datasets used in this study are available in Gene Expression Omnibus (GEO) under accession code GSE140228 (https://www.ncbi.nlm.nih.gov/geo/query/acc.cgi?acc=GSE140228) [82], GSE208253 (https://www.ncbi.nlm.nih.gov/geo/query/acc.cgi?acc=GSE208253), [83] GSE225857 (https://www.ncbi.nlm.nih.gov/geo/query/acc.cgi?acc=GSE225857) [84], GSE236581 (https://www.ncbi.nlm.nih.gov/geo/query/acc.cgi?acc=GSE236581), [85] GSE127465 (https://www.ncbi.nlm.nih.gov/geo/query/acc.cgi?acc=GSE127465) [86], GSE131907 (https://www.ncbi.nlm.nih.gov/geo/query/acc.cgi?acc=GSE131907) [87], GSE279219 (https://www.ncbi.nlm.nih.gov/geo/query/acc.cgi?acc=GSE279219) [88], and GSE279781 (https://www.ncbi.nlm.nih.gov/geo/query/acc.cgi?acc=GSE279781) [89] and Genome Sequence Archive at the National Genomics Data Center (Beijing, China) under accession code PRJCA007744 (https://ngdc.cncb.ac.cn/bioproject/browse/PRJCA007744) [90], PRJCA005422 (https://ngdc.cncb.ac.cn/bioproject/browse/PRJCA005422) [91], HRA003483 (https://ngdc.cncb.ac.cn/gsa-human/browse/HRA003483) [92], and HRA000437 (https://ngdc.cncb.ac.cn/gsa-human/browse/HRA000437) [93]. The Fluorescence images are available on Figshare (https://doi.org/10.6084/m9.figshare.31615864) [94].

Declarations

Competing interests
The authors declare no competing interests.

Received: 11 August 2025 Accepted: 13 March 2026
Published online: 24 March 2026

References

1. Armingol E, Officer A, Harismendy O, Lewis NE. Deciphering cell–cell interactions and communication from gene expression. Nat Rev Genet. 2021;22:71–88.
2. Zhou, X. et al. Circuit design features of a stable two-cell system. Cell. 2018;172:744–757. e717.
3. Rouault H, Hakim V. Different cell fates from cell-cell interactions: core architectures of two-cell bistable networks. Biophys J. 2012;102:417–26.
4. Almet AA, Cang Z, Jin S, Nie Q. The landscape of cell–cell communication through single-cell transcriptomics. Curr Opin Syst Biol. 2021;26:12–23.
5. Türei D, Korcsmáros T, Saez-Rodriguez J. OmniPath: guidelines and gateway for literature-curated signaling pathway resources. Nat Methods. 2016;13:966–7.
6. Efremova M, Vento-Tormo M, Teichmann SA, Vento-Tormo R. CellPhoneDB: inferring cell–cell communication from combined expression of multi-subunit ligand–receptor complexes. Nat Protoc. 2020;15:1484–506.
7. Ramilowski JA, et al. A draft network of ligand–receptor-mediated multicellular signalling in human. Nat Commun. 2015;6:7866.
8. Türei D, et al. Integrated intra- and intercellular signaling knowledge for multicellular omics analysis. Mol Syst Biol. 2021;17:e9923.
9. Luo J, Deng M, Zhang X, Sun X. ESICCC as a systematic computational framework for evaluation, selection, and integration of cell-cell communication inference methods. Genome Res. 2023;33:1788–805.
10. Noël F, et al. Dissection of intercellular communication using the transcriptome-based framework ICELLNET. Nat Commun. 2021;12:1089.
11. Cabello-Aguilar S, et al. SingleCellSignalR: inference of intercellular networks from single-cell transcriptomics. Nucleic Acids Res. 2020;48:e55–e55.
12. Raredon, M. S. B. et al. Comprehensive visualization of cell–cell interactions in single-cell and spatial transcriptomics with NICHES. Bioinform. 2023;39:btac775.
13. Wilk AJ, Shalek AK, Holmes S, Blish CA. Comparative analysis of cell–cell communication at single-cell resolution. Nat Biotechnol. 2024;42:470–83.
14. Cillo, A. R. et al. Immune landscape of viral-and carcinogen-driven head and neck cancer. Immunity. 2020;52:183–199:e189.
15. Jin S, et al. Inference and analysis of cell-cell communication using CellChat. Nat Commun. 2021;12:1088.
16. Troulé, K. et al. CellPhoneDB v5: inferring cell-cell communication from single-cell multiomics data. arXiv preprint 2023 arXiv:2311.04567.
17. Wang, Y. et al. iTALK: an R package to characterize and illustrate intercellular communication. BioRxiv. 2019;507871.
18. Armingol E, Baghdassarian HM, Lewis NE. The diversification of methods for studying cell–cell interactions and communication. Nat Rev Genet. 2024;25:381–400.
19. Dimitrov D, et al. LIANA+ provides an all-in-one framework for cell–cell communication inference. Nat Cell Biol. 2024;26:1613–22.
20. Dimitrov D, et al. Comparison of methods and resources for cell-cell communication inference from single-cell RNA-Seq data. Nat Commun. 2022;13:3224.

21. Wang X, Almet AA, Nie Q. The promising application of cell-cell interaction analysis in cancer from single-cell and spatial transcriptomics. Semin Cancer Biol. 2023;95:42–51.
22. Khosla P, et al. Supervised contrastive learning. Adv Neural Inf Process Syst. 2020;33:18661–73.
23. Zhang Q, et al. Landscape and dynamics of single immune cells in hepatocellular carcinoma. Cell. 2019;179:829-845.e820.
24. Wu R, et al. Comprehensive analysis of spatial architecture in primary liver cancer. Sci Adv. 2021;7:eabg3750.
25. Arora R, et al. Spatial transcriptomics reveals distinct and conserved tumor core and edge architectures that predict survival and targeted therapy response. Nat Commun. 2023;14:5029.
26. Wang F, et al. Single-cell and spatial transcriptome analysis reveals the cellular heterogeneity of liver metastatic colorectal cancer. Sci Adv. 2023;9:eadf5464.
27. Hao Y, et al. Dictionary learning for integrative, multimodal and scalable single-cell analysis. Nat Biotechnol. 2024;42:293–304.
28. Xue R, et al. Liver tumour immune microenvironment subtypes and neutrophil heterogeneity. Nature. 2022;612:141–7.
29. Zheng X, et al. Single-cell analyses implicate ascites in remodeling the ecosystems of primary and metastatic tumors in ovarian cancer. Nat Cancer. 2023;4:1138–56.
30. Yan N, et al. Single-cell transcriptomic analysis reveals tumor cell heterogeneity and immune microenvironment features of pituitary neuroendocrine tumors. Genome Med. 2024. https://doi.org/10.1186/s13073-023-01267-3.
31. Dekker E, Tanis PJ, Vleugels JLA, Kasi PM, Wallace MB. Colorectal cancer. Lancet. 2019;394:1467–80.
32. Chen Y, et al. Spatiotemporal single-cell analysis decodes cellular dynamics underlying different responses to immunotherapy in colorectal cancer. Cancer Cell. 2024;42:1268-1285.e1267.
33. Lv J, et al. Tertiary lymphoid structures in colorectal cancer. Ann Med. 2024;56:2400314.
34. Gao J, et al. Neoadjuvant PD-L1 plus CTLA-4 blockade in patients with cisplatin-ineligible operable high-risk urothelial carcinoma. Nat Med. 2020;26:1845–51.
35. Helmink BA, et al. B cells and tertiary lymphoid structures promote immunotherapy response. Nature. 2020;577:549–55.
36. Cabrita R, et al. Tertiary lymphoid structures improve immunotherapy and survival in melanoma. Nature. 2020;577:561–5.
37. Petitprez F, et al. B cells are associated with survival and immunotherapy response in sarcoma. Nature. 2020;577:556–60.
38. Shen S, et al. Toll-like receptor agonists promote the formation of tertiary lymphoid structure and improve anti-glioma immunity. Neuro Oncol. 2024. https://doi.org/10.1093/neuonc/noae167.
39. Shu, D. H. et al. Immunotherapy response induces divergent tertiary lymphoid structure morphologies in hepatocellular carcinoma. Nat Immunol. 2024;25:2110–23.
40. Sun G, Liu Y. Tertiary lymphoid structures in ovarian cancer. Front Immunol. 2024;15:1465516.
41. Fridman WH, et al. Tertiary lymphoid structures and B cells: an intratumoral immunity cycle. Immunity. 2023;56:2254–69.
42. Yin X, et al. Tobacco exposure primes the secretion of CCL21 positively associated with tertiary lymphoid structure and response to immunotherapy. J Immunother Cancer. 2023. https://doi.org/10.1136/jitc-2023-006939.
43. Zhang, Y. et al. CCL19-producing fibroblasts promote tertiary lymphoid structure formation enhancing anti-tumor IgG response in colorectal cancer liver metastasis. Cancer Cell. 2024:42;370–1385;e1379.
44. Chelvanambi M, Fecek RJ, Taylor JL, Storkus WJ. STING agonist-based treatment promotes vascular normalization and tertiary lymphoid structure formation in the therapeutic melanoma microenvironment. J Immunother Cancer. 2021. https://doi.org/10.1136/jitc-2020-001906.
45. Motwani M, Pesiridis S, Fitzgerald KA. DNA sensing by the cGAS–STING pathway in health and disease. Nat Rev Genet. 2019;20:657–74.
46. Lanng KRB, Lauridsen EL, Jakobsen MR. The balance of STING signaling orchestrates immunity in cancer. Nat Immunol. 2024;25:1144–57.
47. Colbeck EJ, Ager A, Gallimore A, Jones GW. Tertiary lymphoid structures in cancer: drivers of antitumor immunity, immunosuppression, or bystander sentinels in disease? Front Immunol. 2017;8:1830.
48. Furtado GC, et al. Lymphotoxin β receptor signaling is required for inflammatory lymphangiogenesis in the thyroid. Proc Natl Acad Sci. 2007;104:5026–31.
49. Zhang Q, et al. ETV4 Mediated Tumor-Associated Neutrophil Infiltration Facilitates Lymphangiogenesis and Lymphatic Metastasis of Bladder Cancer. Adv Sci. 2023;10:e2205613.
50. Soker S, Takashima S, Miao HQ, Neufeld G, Klagsbrun M. Neuropilin-1 is expressed by endothelial and tumor cells as an isoform-specific receptor for vascular endothelial growth factor. Cell. 1998;92:735–45.
51. Hynes RO. Integrins: bidirectional, allosteric signaling machines. Cell. 2002;110:673–87.
52. Chrzanowska-Wodnicka M. Rap1 in endothelial biology. Curr Opin Hematol. 2017;24:248–55.
53. Zhang H, et al. CXCL2/MIF-CXCR2 signaling promotes the recruitment of myeloid-derived suppressor cells and is correlated with prognosis in bladder cancer. Oncogene. 2017;36:2095–104.
54. Zhou Z, et al. Tumor-associated neutrophils and macrophages interaction contributes to intrahepatic cholangiocarcinoma progression by activating STAT3. J Immunother Cancer. 2021. https://doi.org/10.1136/jitc-2020-001946.
55. Zhang L, et al. VEGF-A/neuropilin 1 pathway confers cancer stemness via activating Wnt/β-catenin axis in breast cancer cells. Cell Physiol Biochem. 2017;44:1251–62.
56. Lin Y, et al. Chemerin has a protective role in hepatocellular carcinoma by inhibiting the expression of IL-6 and GM-CSF and MDSC accumulation. Oncogene. 2017;36:3599–608.

57. Liu X, et al. Glutathione S-transferase A1 suppresses tumor progression and indicates better prognosis of human primary hepatocellular carcinoma. J Cancer. 2020;11:83.
58. Fu X, Yang Y, Zhang D. Molecular mechanism of albumin in suppressing invasion and metastasis of hepatocellular carcinoma. Liver Int. 2022;42:696–709.
59. Ng MS, et al. Deterministic reprogramming of neutrophils within tumors. Science. 2024;383:eadf6493.
60. Jaillon S, et al. Neutrophil diversity and plasticity in tumour progression and therapy. Nat Rev Cancer. 2020;20:485–503.
61. Weiss F, Lauffenburger D, Friedl P. Towards targeting of shared mechanisms of cancer metastasis and therapy resistance. Nat Rev Cancer. 2022;22:157–73.
62. Deng H, et al. Single-cell analysis reveals one cancer-associated fibroblasts subtype linked to metastasis in breast cancer: MXRA5 as a potential novel marker for prognosis. Am J Cancer Res. 2024;14:526–44.
63. Thorlacius-Ussing J, et al. The collagen landscape in cancer: profiling collagens in tumors and in circulation reveals novel markers of cancer-associated fibroblast subtypes. J Pathol. 2024;262:22–36.
64. Wu H-J, Hao M, Yeo SK, Guan J-L. FAK signaling in cancer-associated fibroblasts promotes breast cancer cell migration and metastasis by exosomal miRNAs-mediated intercellular communication. Oncogene. 2020;39:2539–49.
65. Kay EJ, Koulouras G, Zanivan S. Regulation of extracellular matrix production in activated fibroblasts: roles of amino acid metabolism in collagen synthesis. Front Oncol. 2021;11:719922.
66. Takeuchi A, et al. CRTAM determines the CD4+ cytotoxic T lymphocyte lineage. J Exp Med. 2016;213:123–38.
67. Lu TT, Browning JL. Role of the lymphotoxin/LIGHT system in the development and maintenance of reticular networks and vasculature in lymphoid tissues. Front Immunol. 2014;5:47.
68. Deuss FA, Gully BS, Rossjohn J, Berry R. Recognition of nectin-2 by the natural killer cell receptor T cell immunoglobulin and ITIM domain (TIGIT). J Biol Chem. 2017;292:11413–22.
69. Amsellem-Ouazana D, et al. Gene expression profiling of ERBB receptors and ligands in human transitional cell carcinoma of the bladder. J Urol. 2006;175:1127–32.
70. Pang J, et al. Integrating single-cell RNA-seq to construct a Neutrophil prognostic model for predicting immune responses in non-small cell lung cancer. J Transl Med. 2022;20:531.
71. Zilionis R, et al. Single-cell transcriptomics of human and mouse lung cancers reveals conserved myeloid populations across individuals and species. Immunity. 2019;50:1317-1334.e1310.
72. Ligorio, F. et al. Early downmodulation of tumor glycolysis predicts response to fasting-mimicking diet in triple-negative breast cancer patients. Cell Metab. 2024;37:330–44.e7.
73. Montagne, J. M. et al. CD137 agonism enhances anti-PD1 induced activation of clonally expanded CD8+ T cells in a neoadjuvant pancreatic cancer clinical trial. iScience. 2024;28(1):111569.
74. Moses L, Pachter L. Museum of spatial transcriptomics. Nat Methods. 2022;19:534–46.
75. Shao X, et al. Knowledge-graph-based cell-cell communication inference for spatially resolved transcriptomic data with SpaTalk. Nat Commun. 2022;13:4429.
76. Dries R, et al. Giotto: a toolbox for integrative analysis and visualization of spatial expression data. Genome Biol. 2021;22:1–31.
77. Garcia-Alonso L, Holland CH, Ibrahim MM, Turei D, Saez-Rodriguez J. Benchmark and integration of resources for the estimation of human transcription factor activities. Genome Res. 2019;29:1363–75.
78. Marbach D, et al. Wisdom of crowds for robust gene network inference. Nat Methods. 2012;9:796–804.
79. Huynh-Thu VA, Irrthum A, Wehenkel L, Geurts P. Inferring regulatory networks from expression data using tree-based methods. PLoS One. 2010;5:e12776.
80. Jin, Z. et al. scComm: a contrastive learning framework for deciphering cell-cell communications at single-cell resolution. GitHub. 2026 https://github.com/ZijieJin/scComm.
81. Jin Z, et al. scComm: a contrastive learning framework for deciphering cell-cell communications at single-cell resolution. 2026. Zenodo. https://doi.org/10.5281/zenodo.18946992.
82. Zhang, Q. et al. Landscape and Dynamics of Single Immune Cells in Hepatocellular Carcinoma. Dataset. Gene Expression Omnibus. 2022 https://www.ncbi.nlm.nih.gov/geo/query/acc.cgi?acc=GSE140228.
83. Arora, R. et al. Spatial transcriptomics reveals distinct and conserved tumor core and edge architectures that predict survival and targeted therapy response. Dataset. Gene Expression Omnibus. 2023 https://www.ncbi.nlm.nih.gov/geo/query/acc.cgi?acc=GSE208253.
84. Wang, F. et al. Single-cell and spatial transcriptome analysis reveals the cellular heterogeneity of liver metastatic colorectal cancer. Dataset. Gene Expression Omnibus. 2023 https://www.ncbi.nlm.nih.gov/geo/query/acc.cgi?acc=GSE225857.
85. Chen, Y. et al. Spatiotemporal single-cell analysis decodes cellular dynamics underlying different responses to immunotherapy in Colorectal Cancer. Dataset. Gene Expression Omnibus. 2024 https://www.ncbi.nlm.nih.gov/geo/query/acc.cgi?acc=GSE236581.
86. Zilionis, R. et al. Single cell transcriptomics of human and mouse lung cancers reveals conserved myeloid populations across individuals and species. Dataset. Gene Expression Omnibus. 2019 https://www.ncbi.nlm.nih.gov/geo/query/acc.cgi?acc=GSE127465.
87. Kim, N. et al. Single cell RNA sequencing of lung adenocarcinoma. Dataset. Gene Expression Omnibus. 2020 https://www.ncbi.nlm.nih.gov/geo/query/acc.cgi?acc=GSE131907.
88. Ligorio, F. et al. Early downmodulation of tumor glycolysis predicts response to fasting-mimicking diet in triple-negative breast cancer patients. Dataset. Gene Expression Omnibus. 2024 https://www.ncbi.nlm.nih.gov/geo/query/acc.cgi?acc=GSE279219.
89. Montagne, J. et al. CD137 agonism enhances anti-PD1 induced activation of clonally expanded CD8+ T cells in a neoadjuvant pancreatic cancer clinical trial. Dataset. Gene Expression Omnibus. 2024 https://www.ncbi.nlm.nih.gov/geo/query/acc.cgi?acc=GSE279781.
90. Xue, R. et al. scRNA-seq of liver cancer. Dataset. National Genomics Data Center. 2022 https://ngdc.cncb.ac.cn/bioproject/browse/PRJCA007744.

91. Wang, X. et al. single cell sequence of ovarian cancer. Dataset. National Genomics Data Center. 2023 https://ngdc.cncb.ac.cn/bioproject/browse/PRJCA005422.
92. Gu, J. et al. scRNA-seq of Pituitary Tumor. Dataset. National Genomics Data Center. 2023 https://ngdc.cncb.ac.cn/gsa-human/browse/HRA003483.
93. Gu, J. *et al.* Spatial Transcriptomes of Liver Cancer. Dataset. National Genomics Data Center. 2023 https://ngdc.cncb.ac.cn/gsa-human/browse/HRA000437.
94. Jin Z, et al. scComm: a contrastive learning framework for deciphering cell-cell communications at single-cell resolution (mIF). 2026. Figshare. https://doi.org/10.6084/m9.figshare.31615864.

Publisher's Note